# Effect of Polarization on the Band Structure at a Charged Domain Wall in Ferroelectric Materials

A Thesis Submitted to the Committee on Graduate Studies
in Partial Fulfillment of the Requirements for the
Degree of Master of Science in the Faculty of Arts and Science

Trent University
Peterborough, Ontario, Canada

Materials Science M.Sc. Graduate Program
September 2025

# Abstract


## Effect of Polarization on the Band Structure at a Charged Domain Wall in Ferroelectric Materials

Maryam Nasir

The interplay between electron charge, spin, and ferroelectric polarization is under-explored for conducting ferroelectric domain walls (DWs). DWs are interfaces that separate regions (domains) within a material that have different orientations of spontaneous polarization. We investigated the electronic band structure of $t_{2g}$ electrons, confined to 90° charged domain walls (CDWs) in barium titanate ($BaTiO_3$), a prototypical perovskite ferroelectric. A key novel aspect of our study is the explicit inclusion of both orbital and spin degrees of freedom in the Hamiltonian. This leads to an Ising-type spin-orbit coupling (SOC). We constructed a tight-binding (TB) model for $t_{2g}$ electrons that is constrained by symmetries of the DW, including time-reversal, mirror, and rotational symmetries. First-principles density functional theory (DFT) calculations were performed to extract the TB parameters. Our findings offer new insights into spin-orbit interactions at ferroelectric domain walls and open avenues for their potential use in next-generation electronic and spintronic devices.



**Keywords**: Ferroelectrics, Charged Domain Walls, 2DEG, Symmetries, Spintronics, Spin-Orbit Coupling, Polarization, Energy Bands, Hamiltonian, Tight-Binding

# Acknowledgments

This thesis is the result of many months of learning, exploration, and perseverance—an effort that would not have been possible without the unwavering support and kindness of several individuals.

First and foremost, I would like to express my deepest gratitude to my supervisor, Dr. Bill Atkinson, whose patience, humility, and constant encouragement guided me throughout this journey. As an international student from Pakistan adjusting to life and academia in Canada, the transition was challenging. There were moments when I doubted my ability to complete this program, but Dr. Atkinson's steady support and belief in me helped me move forward. I am truly grateful for the opportunity to work under his supervision.

I would also like to sincerely thank my committee members, Dr. Carlo Bradac and Dr. Hendrick de Haan, for their valuable feedback, insights, and guidance throughout my degree. My appreciation extends to my external examiner, Dr. Ganesh Ramachandran, for taking the time to review my work and provide thoughtful comments.

I would also like to gratefully acknowledge the financial support provided by the International Graduate Scholarship and the BMO Entrance Scholarship, which greatly assisted me during my studies.

I am especially thankful to Brennan Cornell, my supervisor's PhD student and my coworker during this time, who was always generous with his time and knowledge. His help

and collaboration over the past two years have been incredibly important to my progress.

I would like to extend heartfelt thanks to my Mr.Husband, whose unwavering support and willingness to embrace a long-distance relationship for the sake of my education meant the world to me. His belief in me kept me going through the most difficult days.

Lastly, I am grateful to my family and friends, near and far, whose love, prayers, and encouragement have been a constant source of strength.

# Contents

# List of Figures

# List of Tables

# List of Abbreviations

| **Abbreviation** | **Full Form** |
|---|---|
| CDW | Charged Domain Wall |
| TB | Tight-Binding |
| SOC | Spin-Orbit Coupling |
| ASOC | Atomic Spin-Orbit Coupling |
| DFT | Density Functional Theory |
| 2DEG | Two-Dimensional Electron Gas |
| $BaTiO_3$ | Barium Titanate |
| TRS | Time-Reversal Symmetry |

Table 1: List of abbreviations used throughout the thesis.

# Chapter 1

# Introduction

## 1.1 Ferroelectricity

Discovered in 1921, ferroelectric materials are distinguished by their ability to exhibit a *spontaneous electric polarization*, a permanent electric dipole moment per unit cell, even in the absence of an external electric field. This spontaneous polarization arises due to a structural phase transition that breaks the inversion symmetry of the crystal, and can be reversed by applying an external electric field. The onset of ferroelectricity in many materials occurs below a critical temperature known as the Curie temperature, $T_c$. Above $T_c$, the crystal structure is typically centrosymmetric (e.g., cubic), and the centers of positive and negative charges coincide, resulting in no net polarization. In this high-temperature phase, the material is said to be in a *paraelectric state*.

As the temperature is reduced below $T_c$, the structure undergoes a phase transition to a lower-symmetry, non-centrosymmetric configuration (e.g., tetragonal or orthorhombic). This symmetry breaking leads to a relative displacement between cations and anions in the unit cell, producing a permanent electric dipole moment and giving rise to spontaneous polarization [2].

The term *ferroelectricity* is named by analogy to *ferromagnetism*, despite the fact that most ferroelectrics do not contain iron. Just as ferromagnetic materials exhibit a spontaneous magnetization due to aligned magnetic dipoles, ferroelectrics exhibit spontaneous polarization due to aligned electric dipoles [3]. The transition from the paraelectric to the

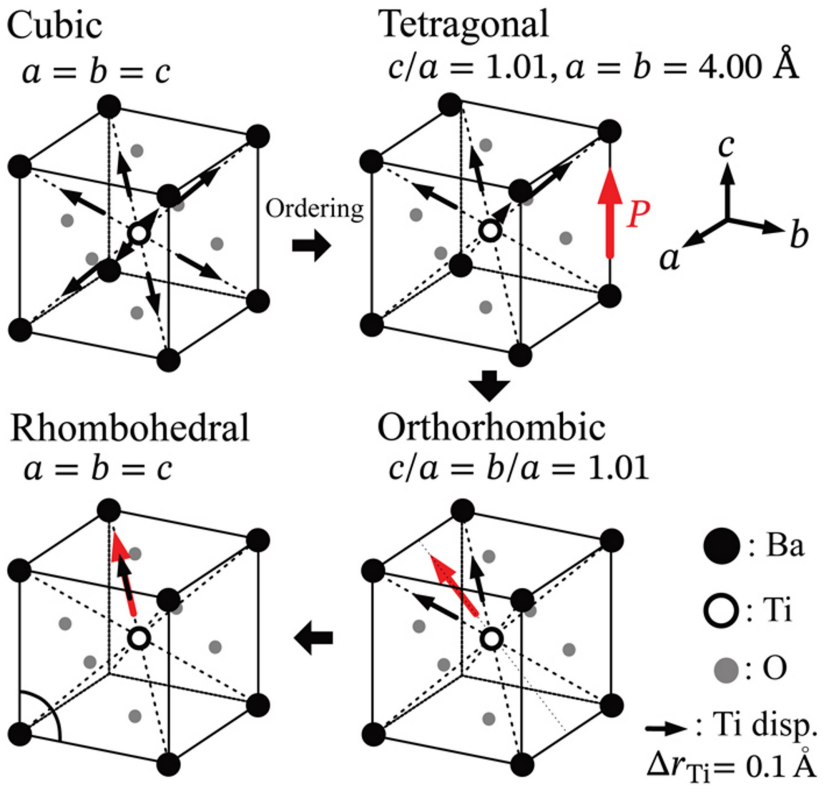


Figure 1.1: Ti ion displacements (black arrows) and resulting polarization (red arrows) in different structural phases of $BaTiO_3$. Phase transitions involve symmetry breaking and lead to ferroelectricity. Adapted with permission from [1].

ferroelectric phase can be described using a Landau-type free energy expansion near the Curie temperature,

$$F(\vec{P}) = F_0 + \frac{1}{2}\alpha(T - T_c)P^2 + \frac{1}{4}\beta P^4 + \frac{1}{6}\gamma P^6 - \vec{E}.\vec{P}, \tag{1.1}$$

where $\vec{P}$ is the polarization, $T$ is the temperature, $\vec{E}$ is the applied electric field, and $\alpha$, $\beta$, and $\gamma$ are material-dependent coefficients. Below $T_c$, the free energy develops a double-well structure, resulting in two stable states with non-zero polarization, corresponding to opposite polarization directions. These states are switchable under an external field, which is the hallmark of ferroelectric behaviour.

A typical feature of ferroelectrics is their *polarization-electric field hysteresis*, which reflects the switching of polarization under a varying external electric field. This behaviour is crucial for applications in non-volatile memory devices, actuators, sensors, and tunable

capacitors [4–7].

### 1.1.1 Ferroelectric Materials

Ferroelectricity is found in many perovskite oxides. A perovskite is characterized by the general formula $ABO_3$ where A and B are positively charged cations and O are oxygen ions (in an octahedral formation). Some well known perovskites are barium titanate ($BaTiO_3$), lead zirconate titanate $Pb(Zr,Ti)O_3$ [8], strontium titanate ($SrTiO_3$) [9] and bismuth ferrite ($BiFeO_3$) [10]. The discovery of ferroelectricity in $BaTiO_3$ in 1946 was a key breakthrough that paved the way for the practical use of ferroelectric materials [11]. In the $BaTiO_3$ structure, $Ba^{2+}$ ions occupy the A-sites, $Ti^{4+}$ ions reside at the B-sites, and $O^{2-}$ ions form an octahedral coordination around the B-site cation as shown in Fig. 1.2. $BaTiO_3$ possesses a high dielectric permittivity, strong piezoelectric response, and good ferroelectric fatigue resistance, making it highly suitable for various device applications. It plays a critical role in multilayer ceramic capacitors, non-volatile ferroelectric random-access memories (FeRAM), piezoelectric sensors, and electro-optic devices [3, 12, 13]. $BaTiO_3$ is one of the most extensively studied and widely used ferroelectric materials, serving as a prototype for understanding perovskite oxides. $BaTiO_3$ offers several advantages, (1) it naturally adopts a tetragonal ferroelectric phase at room temperature, (2) it exhibits a relatively high spontaneous polarization of 20–25 $\mu C/cm^2$, and (3) it shows excellent thermal stability and can be easily tailored for specific applications through chemical doping or atomic substitution [4]. Its strong ferroelectric behavior primarily originates from the $Ti^{4+}$ ions, whose empty $d$ orbitals play a crucial role in enabling off-center displacements that break inversion symmetry [2]. The crystal structure of the perovskite $BaTiO_3$ undergoes a series of phase transitions with decreasing temperature as shown in Fig. 1.1. It changes from the cubic phase to the tetragonal phase at 393 K, then to the orthorhombic phase at 273 K, and finally to the rhombohedral phase at 183 K. The cubic phase is paraelectric, whereas the tetragonal, orthorhombic, and rhombohedral phases are ferroelectric [14]. Each transition involves a distortion of the $TiO_6$ octahedra and a shift of the $Ti^{4+}$ ion from the center, leading to spontaneous polarization along specific crystallographic directions. These structural changes are pivotal to the material's ferroelectric behavior [15, 16].

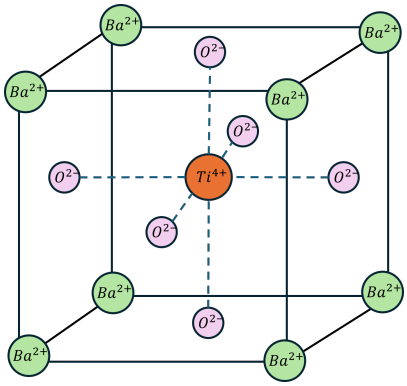


Figure 1.2: Perovskite Bairum Titanate

## 1.2 Domain Walls in Ferroelectrics

In ferroelectric materials, regions of uniform polarization orientation, known as domains, are separated by narrow transition regions called *domain walls*. Domain walls represent nanoscale interfaces where the direction of spontaneous polarization changes abruptly, often giving rise to rich electrostatic and electronic behavior. Fig. 1.3 illustrates the formation of 180° domain walls between regions of different polarization orientation. A 180° domain wall is the boundary between two ferroelectric domains where the polarization points in exactly opposite directions.

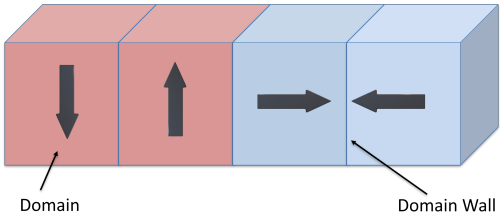


Figure 1.3: Schematic representation of polarization domains and domain walls in a ferroelectric crystal. The arrows represent polarization vectors.

The thickness of these walls depends on the domain wall type and phase of the material. Studies combining high-resolution electron microscopy and theoretical modeling indicate that 90° domain walls in tetragonal $BaTiO_3$ are extremely narrow. A 90° domain wall in a ferroelectric is the boundary between two domains where the spontaneous polarization vec-

tors are perpendicular to each other. For example, Atomic Image Processing measurements report wall widths of approximately 30 Å [1], while electron holography measurements using transmission electron microscopy have specifically determined 90° domain walls in tetragonal $BaTiO_3$ to be 15–25 Å [17].

The change in polarization across a domain wall may lead to a variation in the normal component of polarization. This gives rise to a bound surface charge density, defined as

$$\sigma_b = \vec{P}_1 \cdot \hat{n} - \vec{P}_2 \cdot \hat{n}, \tag{1.2}$$

where $\vec{P}_1$ and $\vec{P}_2$ are the polarization vectors on either side of the wall and $\hat{n}$ is the unit normal vector to the wall pointing into region 2. If $\sigma_b \neq 0$, the domain wall is said to be *charged*; if $\sigma_b = 0$, it is *neutral*.

Charged domain walls (CDW) result in the formation of an internal depolarizing field $\vec{E}_d$, which contributes to the electrostatic energy of the system,

$$U = \frac{1}{2}\varepsilon_0 \int_V |\vec{E}|^2 \, d^3r. \tag{1.3}$$

where $U$ is the total electrostatic energy, $\varepsilon_0$ is the vacuum permittivity, $\vec{E}$ is the electric field (specifically the depolarizing field $\vec{E}_d$), and $V$ is the volume of the ferroelectric material. This relation implies that a strong depolarizing field increases the internal energy of the material, making the CDW energetically unstable unless the bound charges are compensated.

This behavior is further illustrated in Fig. 1.4, which shows a typical head-to-head charged configuration, where opposing domains lead to the accumulation of surface charge and the formation of a depolarizing field. This situation can be understood in simpler terms by drawing an analogy with a capacitor. Just as excess charges on a capacitor's plates generate an internal electric field and store energy, bound charges at a domain wall also come at an energy cost. When two adjacent domains have opposite polarization, they can partially cancel the depolarizing fields, leading to lower overall electrostatic energy.

Fig. 1.5 illustrates several types of domain walls based on the orientation of polariza-

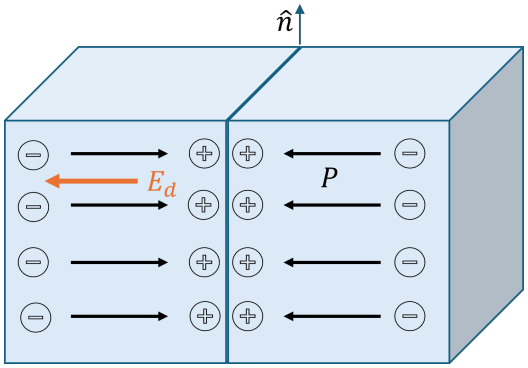


Figure 1.4: Illustration of a charged domain wall showing polarization vectors, bound surface charges, and the resulting depolarizing field $\vec{E}_d$.

tion. In neutral 180° walls [Fig. 1.5(a)], the polarization vectors on either side are exactly opposite but lie parallel to the domain wall plane. Since there is no normal component of polarization across the wall, no bound charge appears. In head-to-head configurations [Fig. 1.5(b)], the polarization vectors point toward the domain wall from both sides. This causes a buildup of *positive bound charge* at the wall. In contrast, tail-to-tail configurations [Fig. 1.5(c)] feature polarization vectors pointing away from the wall, resulting in a *negative bound charge* at the interface. Figure 1.5(d) shows a charged 90° head-to-head domain wall, where the polarization vectors in adjacent domains are perpendicular to each other.

These CDWs are energetically unfavorable unless the bound charges are screened. Re-

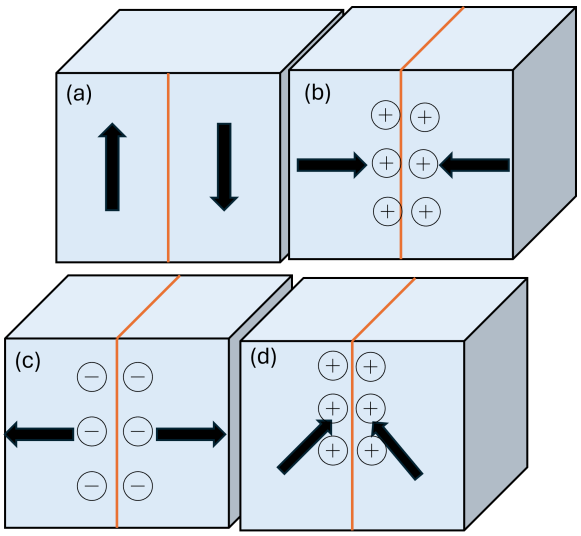


Figure 1.5: Different types of domain walls: (a) 180° (or Kittel) domains with a neutral domain wall (orange line). (b)180° head-to-head configuration, (c)180° tail-to-tail configuration, (d)90° head-to-head configuration.

cent studies have proposed multiple mechanisms for supplying mobile carriers that stabilize CDWs in ferroelectrics. One route involves promoting electrons across the bandgap; however, as demonstrated in perovskite systems, the carrier concentration required to neutralize bound charges at the wall often exceeds the levels achievable through intrinsic excitation alone [18]. Another widely accepted approach involves chemical doping—introducing ionized impurities that donate electrons to the conduction band while forming positively charged ions. These can accumulate at oppositely charged walls, providing localized screening. Such a mechanism is believed to play a role in stabilizing CDWs in bulk $BaTiO_3$ [19]. Notably, positively charged walls screened by electrons tend to exhibit much higher conductivity than their negatively charged, ion-compensated counterparts due to the mass and mobility difference between electrons and ions [20]. A third possibility is interfacial charge transfer from adjacent metallic layers. For example, Bristowe *et al.* [21] showed that at the $LaAlO_3/SrTiO_3$ interface, a polar discontinuity drives electronic reconstruction, leading to the emergence of a two-dimensional electron gas (2DEG) that screens the diverging electrostatic potential.

Building on this idea, Atkinson [22] used a combined Landau–Ginzburg–Devonshire and Schrödinger model to show that as the electron density ($n_{2D}$) increases in ferroelectric thin films, conventional Kittel domain patterns evolve into zigzag CDWs. These structures serve to attract mobile electrons, which in turn screen the bound charges and ultimately flatten the domain walls into head-to-head configurations in the high-density limit. Similarly, Cornell *et al.* [23] demonstrated that at low carrier concentrations, electrons remain pinned at surfaces forming Kittel-like morphologies. With increasing carrier density, however, these patterns evolve—first into zigzag walls, and eventually into flat head-to-head structures, highlighting how multiorbital screening and electronic structure govern the stabilization of conductive domain walls.

In this work, we model a domain wall in the orthorhombic phase of $BaTiO_3$, which exhibits 90° domain walls under ambient conditions [1]. These structures correspond to discontinuities in the polarization direction by 90°. Earlier studies have shown that positively charged domain walls in $BaTiO_3$ can display high, metal-like conductivity, reaching values up to $10^9$ times greater than that of the surrounding bulk material [19, 24].

### 1.2.1 Nonvolatile Behavior of Charged Domain Walls

One of the most appealing features of CDWs is their intrinsic nonvolatile nature. Since the polarization configuration that gives rise to these walls is stable in the absence of external fields, the CDW can serve as a persistent state variable in memory applications. Li *et al.* [25] demonstrated the controlled creation and erasure of CDWs enabled binary logic states that remain stable over time without continuous power supply.

Additionally, the work by Seidel *et al.* [26] on conductive domain walls in multiferroic materials supports the idea that CDWs can be reversibly written and erased through poling. Poling is a process in which an external electric field is applied to a ferroelectric material to align the electric dipoles, effectively setting or switching the polarization direction. This ability to control the domain formation leads to a reliable form of memory where the domain configuration itself encodes information.

Beyond stability, the ability to move or reconfigure domain walls under external stimuli is critical for their integration into devices. Various studies have explored the motion of ferroelectric DWs under applied electric fields, mechanical stress, and scanning probe techniques. Bednyakov *et al.* [27] demonstrated electric-field-driven motion of charged 90° walls in $BaTiO_3$ single crystals.

Piezo-force microscopy (PFM) studies have shown that CDWs can be manipulated through localized voltage pulses, allowing fine spatial control over their formation and position. These findings open the door to dynamic, reconfigurable device architectures where CDWs can function as tunable conductive paths or nanoscale memory elements [28].

### 1.2.2 Evidence of 90° Domain Walls in $BaTiO_3$

$BaTiO_3$ exhibits several types of domain wall geometries, including 90°, 180°, and 71° walls,arising from the symmetry-allowed orientations of spontaneous polarization vectors across the wall. Depending on this orientation, DWs can be classified as *head-to-head*, *tail-to-tail*, or *head-to-tail*. In *head-to-head* configurations, polarization vectors on both sides of the wall point toward the interface, leading to a positive bound charge accumulation. In *tail-to-tail* configurations, the vectors point away from the wall, resulting in negative bound

charge. In contrast, *head-to-tail* walls are charge-neutral, as the polarization vectors are continuous across the boundary.

Among these, 90° CDWs —especially the *head-to-head* type—are of particular interest due to the sharp polarization discontinuity, which gives rise to bound charges and a diverging electrostatic potential. This potential, when screened by mobile carriers, can induce localized conduction. Sluka *et al.* [19] confirmed the existence of a quasi–free-electron gas at such *head-to-head* 90° DWs using scanning probe techniques, revealing a conductivity enhancement of up to $10^9$ compared to the insulating bulk.

Building on this work, Beccard *et al.* [29] employed nanoscale Hall effect measurements and reported relatively low carrier densities ( $10^3$ cm$^{-2}$) and mobilities at head-to-head 90° domain walls in $BaTiO_3$ single crystals—values small to account for complete screening of the bound charge. These findings not only confirm the presence of a two-dimensional electron gas (2DEG) at the wall but also demonstrate its excellent transport characteristics, making it a promising candidate for oxide electronics.

More recently, Bednyakov *et al.* [30] directly visualized the spontaneous formation and evolution of charged 90° head-to-head domain walls in $BaTiO_3$ using in situ optical microscopy. Their observations across the tetragonal-to-orthorhombic phase transition revealed that these walls can fragment and persist below the transition temperature, providing compelling evidence that such charged configurations can form and remain stable under realistic thermodynamic conditions.

## 1.3 Spin-Orbit Physics

Spin–orbit coupling (SOC) is a relativistic quantum phenomenon that describes the interaction between an electron's spin and its orbital motion around the nucleus. At its core, SOC arises when a moving electron experiences an effective magnetic field due to an electric field from the atomic nucleus in the electron's frame of reference. In classical terms, this magnetic field takes the form,

$$\vec{B}_{\text{eff}} \propto \frac{\vec{v} \times \vec{E}}{c^2}, \tag{1.4}$$

where $\vec{v}$ is the velocity of the electron, $\vec{E} = -\nabla V(\vec{r})$ is the electric field arising from the crystal potential $V(\vec{r})$, and $c$ is the speed of light.

This effective field couples to the electron's spin magnetic moment,

$$\vec{\mu}_S = -g\frac{e}{2m}\vec{S}, \tag{1.5}$$

where $\vec{S}$ is the spin angular momentum, $e$ is the elementary charge, $m$ is the electron mass, and $g$ is the Landé $g$-factor. The interaction energy is then given by,

$$H_{\text{int}} = -\vec{\mu}_S \cdot \vec{B}_{\text{eff}}. \tag{1.6}$$

A deeper understanding of SOC emerges from relativistic quantum mechanics, where the Dirac equation naturally incorporates spin degrees of freedom. By performing a non-relativistic expansion of the Dirac equation up to second order, one obtains an effective SOC term in the electron Hamiltonian [31],

$$H_{\text{SO}} = \frac{\hbar}{(2m_0c)^2}(\vec{\nabla}U(\vec{r}) \times \vec{p}) \cdot \vec{\tau}, \tag{1.7}$$

where $\vec{p}$ is the momentum operator, $\vec{\tau}$ are the Pauli matrices, $\hbar$ is the reduced Planck constant, and $U(\vec{r})$ is the electrostatic potential energy. This term describes how the electron's motion through a spatially varying potential couples to its spin. Atomic spin-orbit coupling (ASOC) Hamiltonian is expressed as,

$$H_{\text{SO}}^{\text{atom}} = \xi(r)\,\vec{L} \cdot \vec{S}, \tag{1.8}$$

where $\vec{L}$ is the orbital angular momentum and $\vec{S}$ is the spin angular momentum operator,$\xi(r)$ is a radial SOC strength function. In solid-state systems, the atomic-level interaction described above becomes modified and enhanced by the crystalline environment. Crystal symmetries, broken inversion centers, and collective electronic behavior transform the simple atomic picture into more complex phenomena collectively termed spin-orbit coupling (SOC) in solids. Unlike ASOC, which is purely an atomic property, SOC in crystals de-

pends critically on crystal symmetry, presence or absence of inversion symmetry, Interface and surface effects.This SOC can lead to splitting of electronic bands even in the absence of external magnetic fields.

Two prominent manifestations of SOC are the Dresselhaus and the Rashba SOC effect [32, 33]. The Rashba effect originates from structural inversion asymmetry, which commonly occurs in several situations such as at interfaces between different materials, at crystal surfaces, in the presence of external electric fields etc. When electrons move through such asymmetric environments, they experience an effective magnetic field due to relativistic effects. This leads to the Rashba spin-orbit coupling, described by the Hamiltonian,

$$H_R = \alpha(k_y\tau_x - k_x\tau_y) \tag{1.9}$$

Here, $\alpha$ represents the Rashba coupling strength, $\vec{k} = (k_x, k_y)$ is the electron's momentum in the plane, and $\tau$ are the Pauli spin matrices.

The Rashba effect produces a characteristic "helical" spin texture where electron spins are locked perpendicular to their momentum direction. In contrast, the Dresselhaus effect stems from bulk inversion asymmetry, which is an intrinsic property of certain crystal structures. This effect is particularly prominent in semiconductors with zinc-blende crystal structures, such as gallium arsenide (GaAs) and indium arsenide (InAs).

The two-dimensional Dresselhaus Hamiltonian takes the form,

$$H_D = \beta(k_x\tau_x - k_y\tau_y) \tag{1.10}$$

where $\beta$ is the Dresselhaus coupling constant, determined by the crystal's inherent asymmetry.

Unlike the Rashba effect, Dresselhaus SOC cannot be easily tuned by external fields since it arises from the fundamental crystal structure. The resulting spin texture differs from Rashba SOC, with spins oriented along the crystal's natural symmetry directions.

Understanding and controlling SOC is central to the field of spintronics, where the spin of electrons, rather than their charge alone, is exploited for information storage and process-

ing. SOC enables the conversion between charge and spin currents through mechanisms such as the spin Hall effect, inverse spin galvanic effect (also known as the Edelstein effect), and their counterparts [32]. These interconversion mechanisms offer pathways to develop low-power, high-speed, and non-volatile electronic devices [34–36]. For example, spin–orbit torque magnetic memory (SOT-MRAM) utilizes the spin Hall effect to achieve efficient magnetization switching with ultra-low power consumption [37].

Ferroelectric materials are a great fit for spintronic devices because they naturally link charge, lattice, orbital, and spin properties. Their built-in electric fields can change things like carrier density, band structure, and spin–orbit coupling in nearby materials. What makes them even more attractive is that ferroelectric switching consumes significantly less energy than magnetic switching; for instance, it can require up to a thousand times less power than spin-torque-based devices, making ferroelectrics a highly energy-efficient choice for future spintronic technologies [38].

In perovskite oxides and other *d*-electron systems, SOC exhibits rich orbital-dependent behaviors. For example, in 2DEGs at oxide interfaces such as $LaAlO_3/SrTiO_3$, SOC not only causes Rashba splitting but also depends strongly on the orbital character of the $t_{2g}$ states [39]. Tight-binding and first-principles studies have shown that external electric fields and orbital mixing (e.g., *d–p* or *d–f* hybridization) significantly influence the Rashba coefficient [40].

Another important manifestation is *Ising-type SOC*, which arises in systems that break local inversion symmetry while preserving time-reversal symmetry, such as in certain ferroelectric heterostructures or layered transition metal dichalcogenides (TMDs). In contrast to Rashba or Dresselhaus SOC, Ising SOC pins electron spins along a fixed axis (typically out-of-plane), independent of momentum. It can be expressed as,

$$H_{\text{Ising}} = \lambda_I \tau_z, \tag{1.11}$$

where $\lambda_I$ is the Ising SOC strength and $\tau_z$ is the Pauli spin matrix in the out-of-plane direction. This form of SOC is especially relevant in non-centrosymmetric layered materials, where it plays a crucial role in stabilizing spin-polarized electronic states and unconventional

superconductivity.

## 1.4 Motivation

Our work focuses on exploring the electronic and spin properties that emerge at stable 90° head-to-head charged domain walls in tetragonal $BaTiO_3$. The central question we address in this study is,

> **What is the effect of polarization on the two-dimensional electron gas (2DEG) and the band structures at charged domain walls in ferroelectric $BaTiO_3$?**

Answering this requires detailed modeling of the domain wall environment using tight-binding Hamiltonians constrained by symmetry, and analyzing the consequences for spin, orbital character, and electronic reconstruction.

## 1.5 Thesis Outline

This thesis is structured as follows:

- **Chapter 2** presents the full theoretical framework developed for this study. Here, we construct a detailed tight-binding Hamiltonian for the three $t_{2g}$ conduction bands in $BaTiO_3$, incorporating the effects of polarization, orbital anisotropy, and atomic spin-orbit coupling. This chapter outlines the step-by-step derivation of the Hamiltonian, constrained by symmetry, and forms the core of our modeling approach.

- **Chapter 3** focuses on the numerical results obtained from our model. We present and analyze the calculated band structures, Fermi surfaces, and spin expectation values, highlighting key features such as band splitting, orbital character, and momentum-dependent spin textures. The results are discussed in the context of symmetry-breaking effects and their implications for spintronics applications.

- **Chapter 4** provides concluding remarks and reflections. We summarize the main findings, revisit the assumptions and limitations of our approach, and suggest possible

directions for future research—particularly in developing realistic device architectures based on ferroelectric domain walls.

# Chapter 2

# Theory

## 2.1 Introduction

This chapter outlines the theoretical framework for studying how polarization influences the band structure of a 2DEG with both charge and spin degrees of freedom. The focus is on CDWs in ferroelectric materials, particularly in $BaTiO_3$. To explore this, we construct a tight-binding (TB) Hamiltonian that incorporates the effects of ferroelectric polarization, orbital mixing, and spin-orbit interactions. We analyze how crystalline symmetries constrain the allowed terms in the Hamiltonian and derive symmetry-allowed expressions for each matrix element. These analytical expressions form the basis for understanding spin splitting, orbital anisotropy, and the emergence of Ising-type spin–orbit coupling.

In chapter 3, we solve the developed Hamiltonian and compare its results with density functional theory (DFT) calculations to extract fitting parameters. Using these parameters, we compute the electronic band structures, Fermi surfaces, and spin textures of the 2DEG at the CDW.

## 2.2 Modeling the domain wall

Having discussed the basic physics of ferroelectricity and domain walls in Chapter 1, we now turn to constructing a microscopic model for the conducting 2DEG that forms at a CDW in $BaTiO_3$. Our aim is to develop a TB Hamiltonian that captures the essential ingredients

governing the electronic structure of this 2DEG, including the effects of polarization, orbital degrees of freedom, and spin–orbit interactions.

The model system we consider is a 90° head-to-head domain wall formed between two orthorhombic domains. The coordinate system is defined such that [100] corresponds to the $x$-axis, [010] to the $y$-axis, and [001] to the out-of-plane $z$-axis. As shown in Fig. 2.1, the polarization vectors away from the domain wall lie in the $xz$-plane and point along the [101] and [10$\bar{1}$] directions, respectively. At the center of the wall, the polarization aligns along [100], defining the local direction of the ferroelectric polarization field. We focus on this central region, which behaves like a narrow tetragonal phase sandwiched between two orthorhombic domains.

The rotation of polarization across the wall leads to bound charges, which are electrostati-

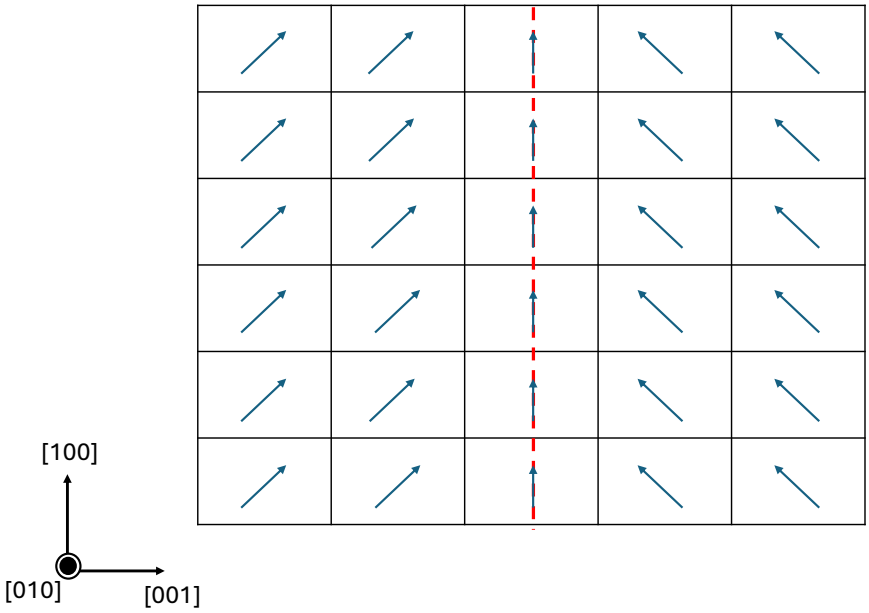


Figure 2.1: Illustration of a 90° head-to-head domain wall in the orthorhombic phase. The two adjacent domains exhibit polarization along the [101] and [10$\bar{1}$] directions, respectively, while the polarization within the domain wall region rotates to align along the [100] axis, forming a conducting interface.

cally compensated by a 2DEG that forms precisely at the interface. It is important to note

that this type of gradual in-plane rotation defines a Néel-type domain wall configuration in ferroelectrics. To describe this 2DEG microscopically, we write a TB Hamiltonian projected onto the Ti $t_{2g}$ orbital basis—specifically the $d_{xy}$, $d_{yz}$, and $d_{zx}$ orbitals—which dominate the conduction band of $BaTiO_3$ near the Fermi level [41]. These orbitals are centered on the Ti sites.

Since spin effects are central to our study, we include the spin degree of freedom explicitly. This leads to a six-band model (three orbitals $\times$ two spins), which forms a complete basis for describing low-energy physics near the CDW.

As a starting point of our model, we refer to three dimensional first-principles results for bulk $BaTiO_3$ in its tetragonal phase. Figure 2.2(a) shows the corresponding Brillouin zone with high-symmetry paths, and Figure 2.2(b) presents the calculated electronic band structure along these paths. The Fermi energy $E_F$ is set to 0 eV.

In our study, the focus is to construct a theoretical model for the 2DEG that emerges at the CDW in $BaTiO_3$. We specifically aim to reproduce the three conduction bands highlighted in red in Fig. 2.2(b), which lie just above the Fermi level and are primarily derived from Ti $t_{2g}$ orbitals, at the CDW. A key feature of our approach is the explicit incorporation of SOC, which introduces additional band splittings.

While setting up the model, we account for the key symmetries of the system, as they determine which terms are allowed in the Hamiltonian. Fig. 2.3 shows one of the Ti-centered $t_{2g}$ orbitals—$d_{xy}$, $d_{yz}$, and $d_{zx}$—within the perovskite structure of $BaTiO_3$. Each of these orbitals lies in a specific plane: $d_{xy}$ in the $xy$-plane, $d_{yz}$ in the $yz$-plane, and $d_{zx}$ in the $xz$-plane. Because of this, they behave differently under mirror reflections. For example, reflecting across the $xz$-plane (which flips $y \to -y$) changes the sign of the $d_{xy}$ and $d_{yz}$ orbitals but leaves the $d_{zx}$ orbital unchanged. These symmetry properties help us determine the structure of the model. We assume that our system preserves the following symmetries:

- **Mirror symmetry in the $xy$-plane**, which corresponds to reflections across the horizontal plane ($z \to -z$),($P_x \to P_x$)
- **Mirror symmetry in the $xz$-plane**, corresponding to reflections across the vertical plane along $y$ ($y \to -y$),($P_x \to P_x$)

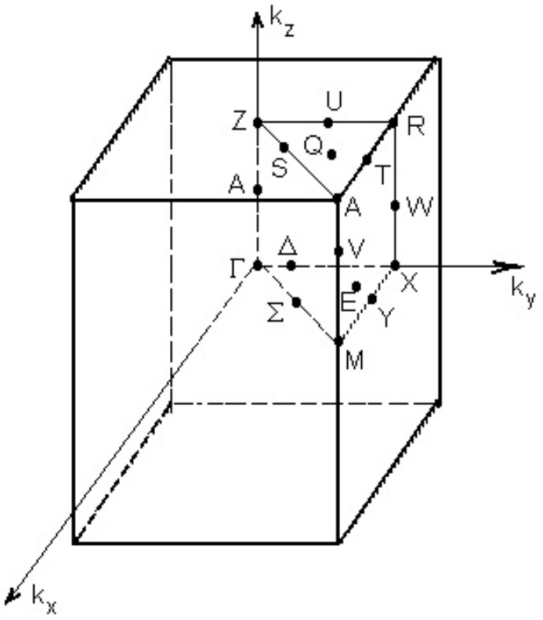


(a)

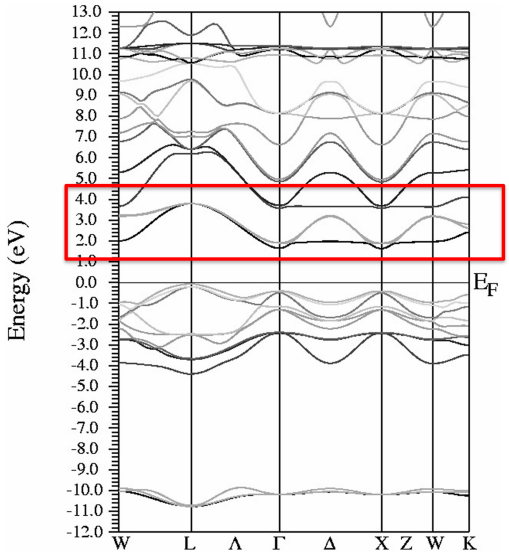


(b)

Figure 2.2: (a) First Brillouin zone of tetragonal $BaTiO_3$, showing high-symmetry points used for band structure calculations. (b) Calculated electronic band structure of tetragonal $BaTiO_3$ along the high-symmetry path in the Brillouin zone. The red box highlights the three conduction bands just above the Fermi level, which are primarily derived from Ti $t_{2g}$ orbitals. Together, these plots provide the momentum-space context and dispersion relation used for electronic structure analysis. Adapted with permission from Ref. [41].

- **Mirror symmetry in the $yz$-plane**, corresponding to reflections across the vertical plane along $x$ $(x \to -x)$,$(P_x \to -P_x)$

- **Time-reversal symmetry**, which ensures that the system behaves identically when both momentum and spin are reversed.

These symmetries are typical for domain walls in $BaTiO_3$ [42], and they play a central role in determining the allowed electronic couplings in the Hamiltonian. For example, they restrict which matrix elements are zero, whether a term is real or imaginary, and whether it is even or odd in momentum variables such as $k_x$ and $k_y$.

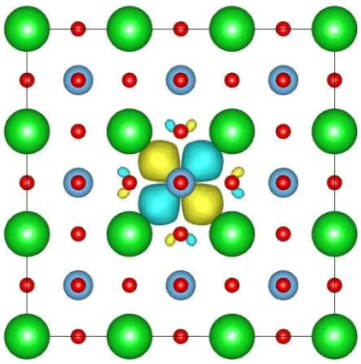

Figure 2.3: Visualization of a Ti-centered $t_{2g}$ orbital ($d_{xy}$, $d_{yz}$, or $d_{zx}$) in the perovskite lattice of $BaTiO_3$. The orientation of a Ti-centered $t_{2g}$ orbital is aligned with the Cartesian coordinate axes and is central to defining the symmetry operations. Adapted with permission from [43].

## 2.3 Hamiltonian Formulation

To describe the electronic structure at the domain wall, we start with the fundamental Hamiltonian for a bulk system expressed as,

$$\hat{H} = -\frac{\hbar^2}{2m}\vec{\nabla}^2 + U(\vec{r}) + \frac{\hbar}{4m^2c^2}\left(\vec{\nabla}U(\vec{r}) \times \vec{p}\right) \cdot \vec{\tau}, \tag{2.1}$$

The Hamiltonian in Eq. (2.1) consists of three main terms: the first term, $-\frac{\hbar^2}{2m}\vec{\nabla}^2$, represents the kinetic energy of the particle; the second term, $U(\vec{r})$, denotes the potential energy due to the external lattice or field; and the third term, $\frac{\hbar}{4m^2c^2}\left(\vec{\nabla}U(\vec{r}) \times \vec{p}\right) \cdot \vec{\tau}$, accounts for the SOC, which captures the interaction between the particle's spin and the electric field gradient arising from the spatial variation of the potential $U(\vec{r})$. Here, $\vec{p} = -i\hbar\vec{\nabla}$ is the canonical momentum operator, and $\vec{\tau} = (\tau_x, \tau_y, \tau_z)$ denotes the vector of Pauli matrices

representing the spin degrees of freedom.

In a practical approach, we represent the Hamiltonian $\hat{H}$ in matrix notation. To do so, we first expand the wave function in terms of a complete and orthonormal set of basis states $|\alpha\vec{k}\rangle$, where $\alpha \in \{d_{xy}, d_{yz}, d_{zx}\}$ labels the orbital character, and $\vec{k} = (k_x, k_y)$ is the two-dimensional crystal momentum vector in the Brillouin zone. Any eigenstate of $\hat{H}$, denoted $|\Psi_{\vec{k}}\rangle$, can then be expressed as a linear combination of these basis states.

$$|\Psi_{\vec{k}}\rangle = \sum_{\alpha} \psi_{\alpha,\vec{k}} |\alpha k\rangle \tag{2.2}$$

where $\psi_{\alpha,\vec{k}}$ are the expansion coefficients. This expansion provides a way to represent the wave function in a discrete basis set, which is essential for numerical calculations. The coefficients $\psi_{\alpha,\vec{k}}$ are the components of the wave function in this basis. Next, we substitute Eq (2.2) into the time-independent Schrödinger equation,

$$\hat{H}|\Psi_k\rangle = E_{\vec{k}}|\Psi_k\rangle, \tag{2.3}$$

which leads to the matrix form of the Schrödinger equation. In this form, Eq. (2.2) becomes,

$$\sum_{\beta} \mathbf{H}_{\alpha\beta,\vec{k}} \psi_{\beta,\vec{k}} = E_{\vec{k}} \psi_{\alpha,\vec{k}} \tag{2.4}$$

where $\mathbf{H}_{\alpha\beta,\vec{k}} = \langle\alpha\vec{k}|\hat{H}|\beta\vec{k}\rangle$ are the Hamiltonian matrix elements. Throughout this thesis, matrix Hamiltonians will be indicated using boldface notation $\mathbf{H}$. These matrix elements correspond to the expected value of the Hamiltonian operator between the basis states $|\alpha\vec{k}\rangle$ and $|\beta\vec{k}\rangle$.

## 2.4 Wannier Functions as a Basis Set

We construct our Hamiltonian using the TB approximation, where the basis consists of localized Wannier orbitals. In $BaTiO_3$, the conduction bands near the Fermi level are primarily derived from the Ti $t_{2g}$ orbitals: $d_{xy}$, $d_{yz}$, and $d_{zx}$.

To describe these orbitals, we write their spatial parts as,

$$\phi^{xy}(\vec{r}) = xy \cdot f(|\vec{r}|), \tag{2.5}$$

$$\phi^{yz}(\vec{r}) = yz \cdot f(|\vec{r}|), \tag{2.6}$$

$$\phi^{zx}(\vec{r}) = zx \cdot f(|\vec{r}|), \tag{2.7}$$

where $f(|\vec{r}|)$ is a radial function that ensures the orbitals are localized around the Ti atoms. We place these Wannier orbitals on a regular lattice, with each orbital centered at a lattice site $\vec{r}_i = (x_i, y_i, 0)$, indicating a two-dimensional lattice structure. The functions are then written as $\phi^{\alpha}(\vec{r} - \vec{r}_i)$, where $\alpha \in \{xy, yz, zx\}$. These orbitals are assumed to satisfy the orthonormality condition,

$$\int d^3r \, \phi^{\alpha}(\vec{r} - \vec{r}_i)^* \phi^{\beta}(\vec{r} - \vec{r}_j) = \delta^{\alpha\beta}\delta_{ij}. \tag{2.8}$$

We then define Bloch states by taking linear combinations of Wannier orbitals over all lattice sites

$$|\alpha\vec{k}\rangle = \frac{1}{\sqrt{N}} \sum_i e^{i\vec{k}\cdot\vec{r}_i} \phi^{\alpha}(\vec{r} - \vec{r}_i), \tag{2.9}$$

where $N$ is the total number of sites and $\vec{k}$ is the crystal momentum. This Bloch basis allows us to express the Hamiltonian in momentum space, where it takes the form of a $6 \times 6$ matrix (three orbitals $\times$ two spins), and is easier to analyze.

To account for the electron's spin, we extend our basis to include spin degrees of freedom. The spin part of the Hilbert space is spanned by two-component spinors, where the spin-up state is represented by $|\uparrow\rangle = \begin{pmatrix} 1 \\ 0 \end{pmatrix}$ and the spin-down state by $|\downarrow\rangle = \begin{pmatrix} 0 \\ 1 \end{pmatrix}$. These spinors form an orthonormal basis for the spin space and are used in conjunction with the orbital basis to construct the full spin-orbital basis states.

## 2.5 Structure of the Effective Spin-Orbital Hamiltonian

We define an effective TB Hamiltonian $\hat{H}$ that acts on a basis of Bloch states including the spin as $|\alpha\vec{k}\sigma\rangle$, where $\sigma$ represents the spin index (up or down) and $\vec{k} = k_x, k_y$. The Hamiltonian in matrix notation is written as

$$\mathbf{H}_{\vec{k}}^{\alpha\sigma,\,\beta\sigma'} = \langle\alpha\sigma\vec{k}|\hat{H}_\mu|\beta\sigma'\vec{k}\rangle = \sum_\mu \mathbf{H}_{\mu,\,\vec{k}}^{\alpha\beta}\,\tau_\mu^{\sigma\sigma'}. \tag{2.10}$$

Here, $\tau_\mu$ represents the $2\times 2$ identity matrix for $\mu = 0$ and the Pauli matrices for $\mu = 1, 2, 3$. The coefficients $\mathbf{H}_{\mu,\,\vec{k}}^{\alpha\beta}$ are the matrix elements in orbital space, and $\tau_\mu$ acts on the spin space. Formally the components for $\mathbf{H}_{\mu,\,\vec{k}}^{\alpha\beta}$ can be obtained by multiplying both sides of Eq. (2.10) by $\tau_\nu^{\sigma'\sigma}$ and summing over spin indices,

$$\frac{1}{2}\sum_{\sigma,\sigma'} \mathbf{H}_{\vec{k}}^{\alpha\sigma,\,\beta\sigma'}\,\tau_\nu^{\sigma'\sigma} = \sum_\mu \frac{1}{2}\mathbf{H}_{\mu,\,\vec{k}}^{\alpha\beta}\sum_{\sigma,\sigma'}\tau_\mu^{\sigma\sigma'}\,\tau_\nu^{\sigma'\sigma}. \tag{2.11}$$

Using the orthogonality relation of Pauli matrices

$$\sum_{\sigma,\sigma'}\tau_\mu^{\sigma\sigma'}\,\tau_\nu^{\sigma'\sigma} = 2\delta_{\mu\nu}, \tag{2.12}$$

and substituting Eq. (2.12) into Eq. (2.11), we obtain

$$\frac{1}{2}\sum_{\sigma,\sigma'} \mathbf{H}_{\vec{k}}^{\alpha\sigma,\,\beta\sigma'}\,\tau_\nu^{\sigma'\sigma} = \mathbf{H}_{\nu,\,\vec{k}}^{\alpha\beta}. \tag{2.13}$$

This gives an explicit expression for the spin-projected component $\mathbf{H}_{\nu,\,\vec{k}}^{\alpha\beta}$ of the Hamiltonian. We can also write this projection compactly as a trace over spin space,

$$\mathbf{H}_{\nu,\,\vec{k}}^{\alpha\beta} = \frac{1}{2}\,\mathrm{Tr}_\sigma\left[\mathbf{H}_{\vec{k}}^{\alpha\sigma,\,\beta\sigma'}\,\tau_\nu\right]. \tag{2.14}$$

Although Eq. (2.14) holds formally, in our approach we will not compute these projections directly. Instead, we will use symmetry arguments to determine which components $H_{\nu,\,\vec{k}}^{\alpha\beta}$ are allowed or constrained by the symmetries. Considering only the orbital part of the

Hamiltonian in Eq. (2.10), we write the general form of the orbital-sector Hamiltonian that we will be working with throughout this study,

$$\mathbf{H}_{\mu,\vec{k}} = \begin{pmatrix} \epsilon^{xy}_{\mu,\vec{k}} & t^{xy,yz}_{\mu,\vec{k}} & t^{xy,xz}_{\mu,\vec{k}} \\ (t^{xy,yz}_{\mu,\vec{k}})^* & \epsilon^{yz}_{\mu,\vec{k}} & t^{yz,xz}_{\mu,\vec{k}} \\ (t^{xy,xz}_{\mu,\vec{k}})^* & (t^{yz,xz}_{\mu,\vec{k}})^* & \epsilon^{xz}_{\mu,\vec{k}} \end{pmatrix}, \tag{2.15}$$

where, $\epsilon^{\alpha}_{\mu,\vec{k}}$ ($\alpha = xy, yz, xz$) are intra-orbital dispersions, $t^{\alpha,\beta}_{\mu,\vec{k}}$ represent inter-orbital hybridizations arising from symmetry-breaking effects such as ferroelectric polarization or structural distortions. The inter-orbital hybridization terms, absent in centrosymmetric crystals, become prominent at ferroelectric domain walls and play a pivotal role in shaping the spin-orbit coupled band structure.

We can write Eq. (2.10) explicitly as,

$$\mathbf{H}_{\vec{k}} = \mathbf{H}_{0,\vec{k}} \otimes \tau_0 + \mathbf{H}_{1,\vec{k}} \otimes \tau_1 + \mathbf{H}_{2,\vec{k}} \otimes \tau_2 + \mathbf{H}_{3,\vec{k}} \otimes \tau_3. \tag{2.16}$$

## 2.6 How Symmetry Constrains the Hamiltonian

Now that we have constructed the Hamiltonian matrix in the form of a tensor product between orbital and spin components as in Eq. (2.16), we turn to the role of symmetry in constraining its structure. If $\hat{O}$ is a symmetry operation of the system, then the total Hamiltonian must satisfy the invariance condition

$$\hat{O}\mathbf{H}_{\vec{k}}\hat{O}^{-1} = \mathbf{H}_{\vec{k}}. \tag{2.17}$$

This condition imposes constraints on the matrix elements of the Hamiltonian, ensuring that only terms compatible with the symmetry are retained. Because the Hamiltonian is defined over both orbital and spin degrees of freedom, the symmetry operator $\hat{O}$ can be factorized as,

$$\hat{O} = \hat{O}_{\text{orb}} \otimes \hat{O}_{\text{sp}}, \tag{2.18}$$

where $\hat{O}_{\text{orb}}$ acts on the orbital space and $\hat{O}_{\text{sp}}$ acts on the spin space. Substituting this into our previously defined Hamiltonian expansion (2.16), we arrive at the symmetry condition,

$$\sum_{\mu}\langle\hat{O}_{\text{orb}}\alpha\vec{k}|\hat{H}_{\mu}|\hat{O}_{\text{orb}}\beta\vec{k}\rangle\otimes\hat{O}_{\text{sp}}^{\dagger}\tau_{\mu}\hat{O}_{\text{sp}}=\pm\sum_{\mu}\langle\alpha\vec{k}|\hat{H}_{\mu}|\beta\vec{k}\rangle\otimes\tau_{\mu}. \tag{2.19}$$

This expression ensures that each term in the Hamiltonian expansion transforms consistently under symmetry operations. We have used the fact that under reflection and time-reversal operations,

$$\hat{O}_{\text{sp}}^{\dagger}\tau_{\mu}\hat{O}_{\text{sp}}=\pm\tau_{\mu} \tag{2.20}$$

where the sign depends on the symmetry. For reflections, the sign is determined by the specific symmetry operation (see Table 2.1), while for time-reversal the sign is negative for $\mu=1,2,3$ and positive for $\mu=0$. As a consequence, the condition $\hat{O}_{\text{orb}}\hat{H}_{\mu,\vec{k}}\hat{O}_{\text{orb}}^{-1}=\pm\hat{H}_{\mu,\vec{k}}$ must hold. Now we will consider spin transformations under reflections through the $xy$, $yz$, and $zx$ planes. To formalize this, we define, $\hat{\sigma}$ as the reflection operator acting on spin space, and $\hat{S}_i$ $(i=x,y,z)$ as the spin operators, represented by $\frac{\hbar\tau_i}{2}$. For simplicity we will take $\hbar=1$.

We define $\hat{\sigma_z}$ as the reflection operator through the xy-plane, such that it acts on spin operators as,

$$\hat{\sigma}_z(\hat{S}_x,\hat{S}_y,\hat{S}_z)\,\hat{\sigma}_z^{\dagger}=(-\hat{S}_x,-\hat{S}_y,\hat{S}_z)$$

where the spin components along the $x$ and $y$ directions change sign, while the $z$ component remains invariant. This transformation can be realized by a $\pi$ rotation about the $z$-axis, implemented by the rotation operator,

$$\hat{R}=e^{-i\hat{S}_z\pi}=-i\tau_3. \tag{2.21}$$

Similarly for yz and zx plane, the spin operators are as given in Table 2.1.

| **Reflection Plane** | **Spin Transformation** | $\hat{O}_{\text{sp}}$ | $\hat{O}_{\text{sp}}\,\tau_\mu\,\hat{O}_{\text{sp}}^{-1}$ |
|---|---|---|---|
| $xy$-plane | $(\hat{S_x}, \hat{S_y}, \hat{S_z}) \to (-\hat{S_x}, -\hat{S_y}, \hat{S_z})$ | $-i\tau_3$ | $\begin{cases} \tau_0, & \mu = 0 \\ -\tau_1, & \mu = 1 \\ -\tau_2, & \mu = 2 \\ \tau_3, & \mu = 3 \end{cases}$ |
| $yz$-plane | $(\hat{S_x}, \hat{S_y}, \hat{S_z}) \to (\hat{S_x}, -\hat{S_y}, -\hat{S_z})$ | $-i\tau_1$ | $\begin{cases} \tau_0, & \mu = 0 \\ \tau_1, & \mu = 1 \\ -\tau_2, & \mu = 2 \\ -\tau_3, & \mu = 3 \end{cases}$ |
| $zx$-plane | $(\hat{S_x}, \hat{S_y}, \hat{S_z}) \to (-\hat{S_x}, \hat{S_y}, -\hat{S_z})$ | $-i\tau_2$ | $\begin{cases} \tau_0, & \mu = 0 \\ -\tau_1, & \mu = 1 \\ \tau_2, & \mu = 2 \\ -\tau_3, & \mu = 3 \end{cases}$ |

Table 2.1: Spin transformations under reflection.

## 2.7 Time-Reversal Symmetry and Its Effect on the Wavefunction

Under TRS, the full wavefunction, which includes both orbital and spin parts, transforms in a well-defined manner. Consider the Bloch state associated with the $d_{xy}$ orbital,

$$\phi_{\vec{k}}^{xy}(x, y, z) = \phi_{\vec{k}}^{xy}(x, y, z) \otimes \chi_{\text{spin}},$$

where $\phi_{\vec{k}}^{xy}$ represents the spatial (orbital) part of the wavefunction at momentum $\vec{k}$, and $\chi_{\text{spin}}$ is the corresponding spinor. Under time reversal, both the momentum and spin degrees of freedom transform as,

$$\hat{T}\phi_{\vec{k}}^{xy}(x, y, z) = \phi_{-\vec{k}}^{xy}(x, y, z) \cdot \hat{T}_{\text{spin}}\chi_{\text{spin}}, \tag{2.22}$$

where $\hat{T}_{\text{spin}} = -i\tau_y\mathcal{K}$ is the spin part of the time-reversal operator, and $\mathcal{K}$ denotes complex conjugation. Let the spinor be expressed as,

$$\chi_{\text{spin}} = \begin{bmatrix} \alpha \\ \beta \end{bmatrix},$$

then under TRS,

$$\hat{T}\chi_{\text{spin}} = -i\tau_y\chi^*_{\text{spin}} = -i\begin{bmatrix}0 & -i\\ i & 0\end{bmatrix}\begin{bmatrix}\alpha^*\\ \beta^*\end{bmatrix} = \begin{bmatrix}-\beta^*\\ \alpha^*\end{bmatrix}.$$

Therefore, the full time-reversed wavefunction becomes,

$$\hat{T}\phi^{xy}_{\vec{k}}(x,y,z) = \phi^{xy}_{-\vec{k}}(x,y,z)\begin{bmatrix}-\beta^*\\ \alpha^*\end{bmatrix}. \tag{2.23}$$

This transformation reflects both momentum reversal and spin rotation. As a result, in a time-reversal symmetric system, the matrix elements of the Hamiltonian must satisfy the constraint,

$$\langle\alpha\vec{k}\sigma|\hat{H}|\beta\vec{k}'\sigma'\rangle = \langle\hat{T}\alpha\vec{k}\sigma|\hat{H}|\hat{T}\beta\vec{k}'\sigma'\rangle^*. \tag{2.24}$$

This condition imposes symmetry constraints on all momentum-dependent hopping terms and determines the allowed structure of the spin-dependent Hamiltonian.

## 2.8 Orbital Hamiltonian for $\mathbf{H}_{0,\vec{k}}$

We now focus on the spin-independent part of the Hamiltonian, $\mathbf{H}_{0,\vec{k}}$. Using Eq. (2.15), we can write

$$\mathbf{H}_{0,\vec{k}} = \begin{bmatrix}\epsilon^{xy}_{0,\vec{k}} & t^{xy,yz}_{0,\vec{k}} & t^{xy,xz}_{0,\vec{k}}\\ (t^{xy,yz}_{0,\vec{k}})^* & \epsilon^{yz}_{0,\vec{k}} & t^{yz,xz}_{0,\vec{k}}\\ (t^{xy,xz}_{0,\vec{k}})^* & (t^{yz,xz}_{0,\vec{k}})^* & \epsilon^{xz}_{0,\vec{k}}\end{bmatrix} \tag{2.25}$$

While all terms in the matrix may, in general, contain contributions from the polarization component $P_x$ , we omit these dependencies here for the sake of simplicity. The full polarization-dependent expressions will be introduced explicitly in later sections, where their role in the physical behavior of the system becomes essential. As $\tau_0$ is invariant under spin-space operations, as we can see from the table 2.1, the transformation properties of $\mathbf{H}_{0,\vec{k}}$ are determined solely by the orbital sector. We will apply all the symmetries on the matrix elements to see how they transform.

**Mirror in the $x$-$z$ plane**

The mirror operation $\hat{\sigma}_y$ maps $y \to -y$. The polarization $P_x$ remains unchanged in this case. Using Eq. (2.9), we get

$$\begin{aligned}
\hat{\sigma}_y \phi^{xy}_{\vec{k}}(x,y,z) &= \phi^{xy}_{\overline{k}}(x,-y,z) \\
&= \frac{1}{\sqrt{N_x N_y}} \sum_{i_x,i_y} (x-x_i)(-y-y_i) f(x-x_i,-y-y_i,z) e^{i(k_x x_i + k_y y_i)} \\
&= -\frac{1}{\sqrt{N_x N_y}} \sum_{i_x,i_y} (x-x_i)(y+y_i) f(x-x_i,y+y_i,z) e^{i(k_x x_i + k_y y_i)} \\
&\quad \text{(using the change of variables: } y_i \to -y_i) \\
&= -\frac{1}{\sqrt{N_x N_y}} \sum_{i_x,i_y} (x-x_i)(y-y_i) f(x-x_i,y-y_i,z) e^{i(k_x x_i - k_y y_i)} \\
&= -\phi^{xy}_{\overline{k}}(x,y,z), \qquad (2.26)
\end{aligned}$$

where $\overline{k} = (k_x, -k_y)$.

Similarly, we can also show that,

$$\hat{\sigma}_y \, \phi^{yz}_{\vec{k}}(x,y,z) = -\phi^{yz}_{\overline{k}}(x,y,z), \qquad (2.27)$$

$$\hat{\sigma}_y \, \phi^{xz}_{\vec{k}}(x,y,z) = \phi^{xz}_{\overline{k}}(x,y,z). \qquad (2.28)$$

**Mirror in the $y$-$z$ plane**

In this case, $\hat{\sigma}_x$ maps $x \to -x$.

$$\begin{aligned}
\hat{\sigma}_x \phi^{xy}_{\vec{k}}(x,y,z) &= \frac{1}{\sqrt{N_x N_y}} \sum_{i_x,i_y} (-x-x_i)(y-y_i) f(-x-x_i,y-y_i,z) e^{i(k_x x_i + k_y y_i)} \\
&= -\frac{1}{\sqrt{N_x N_y}} \sum_{i_x,i_y} (x+x_i)(y-y_i) f(x+x_i,y-y_i,z) e^{i(k_x x_i + k_y y_i)} \\
&\quad \text{(using the change of variables } x_i \to -x_i) \\
&= -\frac{1}{\sqrt{N_x N_y}} \sum_{i_x,i_y} (x-x_i)(y-y_i) f(x-x_i,y-y_i,z) e^{i(-k_x x_i + k_y y_i)} \\
\hat{\sigma}_x \phi^{xy}_{\vec{k}}(x,y,z) &= -\phi^{xy}_{\tilde{k}}(x,y,z), \qquad (2.29)
\end{aligned}$$

where $\tilde{k} = (-k_x, k_y)$. Similarly, we can also show that:

$$\hat{\sigma}_x \phi^{yz}_{\vec{k}}(x,y,z) = +\phi^{yz}_{\tilde{k}}(x,y,z), \tag{2.30}$$

$$\hat{\sigma}_x \phi^{zx}_{\vec{k}}(x,y,z) = -\phi^{zx}_{\tilde{k}}(x,y,z). \tag{2.31}$$

**Mirror in the $x$-$y$ plane**

The mirror operation $\hat{\sigma}_z$ maps $z \to -z$. From this, we get:

$$\begin{aligned} \hat{\sigma}_z \phi^{xy}_{\vec{k}}(x,y,z) &= \phi^{xy}_{\vec{k}}(x,y,-z) \\ &= \phi^{xy}_{\vec{k}}(x,y,z), \end{aligned} \tag{2.32}$$

$$\begin{aligned} \hat{\sigma}_z \phi^{yz}_{\vec{k}}(x,y,z) &= \phi^{yz}_{\vec{k}}(x,y,-z) \\ &= -\phi^{yz}_{\vec{k}}(x,y,z), \end{aligned} \tag{2.33}$$

$$\begin{aligned} \hat{\sigma}_z \phi^{xz}_{\vec{k}}(x,y,z) &= \phi^{xz}_{\vec{k}}(x,y,-z) \\ &= -\phi^{xz}_{\vec{k}}(x,y,z). \end{aligned} \tag{2.34}$$

### 2.8.1 Example of a Matrix Element

To illustrate how symmetry constraints influence the structure of the orbital Hamiltonian $\hat{H}_0$, we examine a specific matrix element corresponding to the hopping between the $d_{yz}$ and $d_{xz}$ orbitals at crystal momentum $\vec{k} = (k_x, k_y)$. This term appears in the $(yz, xz)$ off-diagonal block of the spin-independent part of the Hamiltonian and takes the form

$$t^{yz,xz}_{0,\vec{k}} \otimes \tau_0.$$

By applying reflection symmetry in the $xy$ plane and expressing the matrix element in the form of Eq. (2.19), we obtain

$$\langle \hat{\sigma}_z \, \phi^{yz}_{\vec{k}} \,\big|\, \hat{H}_0 \,\big|\, \hat{\sigma}_z \, \phi^{xz}_{\vec{k}} \rangle \otimes \tau_0. \tag{2.35}$$

Since $\tau_0$ is invariant under spin operations as we can see from 2.1, and based on the symmetry relations given in Eqs. (2.33) and (2.34), this transformation yields

$$\langle \phi^{yz}_{\vec{k}} \,|\, \hat{H}_0 \,|\, \phi^{xz}_{\vec{k}} \rangle. \tag{2.36}$$

implying that the matrix element remains unchanged under reflection. Therefore, we conclude that

$$t^{yz,xz}_{0,\vec{k}}(P_x) = +t^{yz,xz}_{0,\vec{k}}(P_x), \tag{2.37}$$

which indicates that this term is **even** under reflection through the $xy$-plane. Next, we apply these constraints to the Hamiltonian matrix of the $t_{2g}$ orbitals. Under reflection in the $z$-axis (the operation $\hat{\sigma_z}$), the matrix transforms as follows:

$$\begin{bmatrix} \epsilon^{xy}_{0,\vec{k}} & t^{xy,yz}_{0,\vec{k}} & t^{xy,xz}_{0,\vec{k}} \\ (t^{xy,yz}_{0,\vec{k}})^* & \epsilon^{yz}_{0,\vec{k}} & t^{yz,xz}_{0,\vec{k}} \\ (t^{xy,xz}_{0,\vec{k}})^* & (t^{yz,xz}_{0,\vec{k}})^* & \epsilon^{xz}_{0,\vec{k}} \end{bmatrix} \xrightarrow{\hat{\sigma}_z} \begin{bmatrix} \epsilon^{xy}_{0,\vec{k}} & -t^{xy,yz}_{0,\vec{k}} & -t^{xy,xz}_{0,\vec{k}} \\ -(t^{xy,yz}_{0,\vec{k}})^* & \epsilon^{yz}_{0,\vec{k}} & t^{yz,xz}_{0,\vec{k}} \\ -(t^{xy,xz}_{0,\vec{k}})^* & (t^{yz,xz}_{0,\vec{k}})^* & \epsilon^{xz}_{0,\vec{k}} \end{bmatrix}. \tag{2.38}$$

For the matrix to remain invariant under this reflection, the constraints

$$t^{xy,yz}_{0,\vec{k}} = t^{xy,xz}_{0,\vec{k}} = 0$$

must hold. Applying reflection in the $zx$ plane (i.e., the operation $\hat{\sigma}_y$), the reduced Hamiltonian matrix becomes

$$\begin{bmatrix} \epsilon^{xy}_{0,\vec{k}} & 0 & 0 \\ 0 & \epsilon^{yz}_{0,\vec{k}} & t^{yz,xz}_{0,\vec{k}} \\ 0 & (t^{yz,xz}_{0,\vec{k}})^* & \epsilon^{xz}_{0,\vec{k}} \end{bmatrix} \xrightarrow{\hat{\sigma}_y} \begin{bmatrix} \epsilon^{xy}_{0,\overline{k}} & 0 & 0 \\ 0 & \epsilon^{yz}_{0,\overline{k}} & -t^{yz,xz}_{0,\overline{k}} \\ 0 & -(t^{yz,xz}_{0,\overline{k}})^* & \epsilon^{xz}_{0,\overline{k}} \end{bmatrix}. \tag{2.39}$$

where $\overline{k} = (k_x, -k_y)$. This transformation implies that the diagonal terms $\epsilon^{\alpha}_{0,\vec{k}}$ are even functions of $k_y$, while the off-diagonal element $t^{yz,xz}_{0,\vec{k}}$ is odd in $k_y$.

Next, we consider reflection in the $yz$ plane ($\hat{\sigma}_x$) using Eqs. (2.26), (2.27), and (2.28), under

which the Hamiltonian transforms as

$$\begin{bmatrix} \epsilon^{xy}_{0,\vec{k}} & 0 & 0 \\ 0 & \epsilon^{yz}_{0,\vec{k}} & t^{yz,xz}_{0,\vec{k}} \\ 0 & (t^{yz,xz}_{0,\vec{k}})^* & \epsilon^{xz}_{0,\vec{k}} \end{bmatrix} \xrightarrow{\hat{\sigma}_x} \begin{bmatrix} \epsilon^{xy}_{0,\tilde{k}} & 0 & 0 \\ 0 & \epsilon^{yz}_{0,\tilde{k}} & -t^{yz,xz}_{0,\tilde{k}}(-P_x) \\ 0 & \left(-t^{yz,xz}_{0,\tilde{k}}(-P_x)\right)^* & \epsilon^{xz}_{0,\tilde{k}} \end{bmatrix}, \tag{2.40}$$

where $\tilde{k} = (-k_x, k_y)$. This transformation implies that the diagonal terms $\epsilon^{\alpha}_{0,\vec{k}}$ are even functions of $k_x$, while the off-diagonal element $t^{yz,xz}_{0,\vec{k}}$ contains terms that are odd in $k_x$ or $P_x$. Subsequently, applying time-reversal symmetry (TRS), which inverts momentum and complex conjugates all elements, yields

$$\begin{bmatrix} \epsilon^{xy}_{0,\vec{k}} & 0 & 0 \\ 0 & \epsilon^{yz}_{0,\vec{k}} & t^{yz,xz}_{0,\vec{k}}(P_x) \\ 0 & \left(t^{yz,xz}_{0,\vec{k}}(P_x)\right)^* & \epsilon^{xz}_{0,\vec{k}} \end{bmatrix} \xrightarrow{\hat{\mathcal{T}}} \begin{bmatrix} \left[\epsilon^{xy}_{0,-\vec{k}}\right]^* & 0 & 0 \\ 0 & \left[\epsilon^{yz}_{0,-\vec{k}}\right]^* & \left[t^{yz,xz}_{0,-\vec{k}}(P_x)\right]^* \\ 0 & \left[t^{yz,xz}_{0,-\vec{k}}(P_x)\right] & \left[\epsilon^{xz}_{0,-\vec{k}}\right]^* \end{bmatrix}. \tag{2.41}$$

From this, we learn that $\epsilon^{\alpha}_{0,\vec{k}}$ is real and even in $\vec{k}$, and that $t^{\alpha}_{\vec{k}}(P_x)$ may contain real terms that are even in $\vec{k}$ and imaginary terms that are odd in $\vec{k}$.

**Symmetry-Constrained Form:** A general form that satisfies the symmetry constraints for $t^{yz,xz}_{0,(k_x,k_y)}(P_x)$ is given by,

$$t^{yz,xz}_{0,\vec{k}}(P_x) = t^{yz,xz}_{01} \sin(k_x) \sin(k_y) + i t^{yz,xz}_{02} \sin(k_y) P_x. \tag{2.42}$$

This form is constructed using the simplest symmetry-allowed functions—typically trigonometric terms such as $\sin(k_x)$ and $\sin(k_y)$—which are commonly used in tight-binding models. These functions are chosen because they naturally respect the underlying crystal symmetries, including inversion, mirror reflection, and time-reversal symmetry.

The first term, proportional to $t_{01}$, does not depend on $P_x$ and captures purely momentum-dependent hopping. However, in our case, this term is not essential because it primarily contributes to fine-tuning the Fermi surface, which is not the focus of this analysis. Therefore, we omit it in our low-energy effective model.

The second term, $it_{02} \sin(k_y) P_x$, introduces a linear coupling between the momentum and

polarization, reflecting inversion-symmetry breaking due to the ferroelectric distortion along the $x$-direction.

The final matrix can be written as

$$H_{0,k} = \begin{pmatrix} \epsilon_0^{xy} & 0 & 0 \\ 0 & \epsilon_0^{yz} & it_{02}^{yz,zx} s_y P_x + t_{01}^{yz,zx} s_x s_y \\ 0 & -it_{02}^{yz,zx} s_y P_x + t_{01}^{yz,zx} s_x s_y & \epsilon_0^{zx} \end{pmatrix}. \tag{2.43}$$

Here, $s_x$ and $s_y$ denote $\sin k_x$ and $\sin k_y$, respectively. This form explicitly respects all relevant mirror and time-reversal symmetries and includes only the lowest-order allowed couplings between orbitals and polarization.

Now that we have systematically analysed the off-diagonal hopping terms and their behaviour under symmetries, we turn our attention to the diagonal energy terms in the Hamiltonian.

To maintain consistency and completeness in the construction of the tight-binding model, it is essential to apply the same set of symmetries to the diagonal terms as well. These diagonal elements, corresponding to orbital-resolved on-site energies and self-hopping processes, must respect the underlying symmetry constraints of the system to ensure the physical accuracy and predictive reliability of the model.

### 2.8.2 Diagonal terms in $\mathbf{H}_{0,\vec{k}}$

The diagonal elements are determined using the tight-binding approximation. For instance, the matrix element for the $xz$ orbital can be computed as,

$$\epsilon_{0,\vec{k}}^{xz} = \langle xz\vec{k}|\hat{H}|xz\vec{k}\rangle \tag{2.44}$$

Expanding the wave functions in terms of Bloch sums,

$$\epsilon^{xz}_{0,\vec{k}} = \frac{1}{N_x N_y} \sum_{i_x,i_y} \sum_{j_x,j_y} e^{i(k_x x_i + k_y y_i)} e^{-i(k_x x_j + k_y y_j)} \times \int d^3r \left((x - x_i)(z)\right)^* f(x - x_i, y - y_i, z)\, \hat{H}\, (x - x_i)(z) f(x - x_j, y - y_j, z) \quad (2.45)$$

Simplifying:

$$\epsilon^{xz}_{0,\vec{k}} = \frac{1}{N_x N_y} \sum_{i_x,i_y} \sum_{j_x,j_y} e^{i(k_x x_i - k_x x_j + k_y y_i - k_y y_j)} \times \int d^3r ((x - x_i)(z))^* f(x - x_i, y - y_i, z) \hat{H} (x - x_i)(z) f(x - x_j, y - y_j, z) \quad (2.46)$$

The hopping matrix elements are defined as,

$$((x-x_i)(z))^* f(x-x_i, y-y_i, z) \hat{H} (x-x_i)(z) f(x-x_j, y-y_j, z) = \begin{cases} t_0 & \text{if } i = j \\ -t_{\parallel} & \text{if } j_x = i_x \pm 1 \\ -t_{\perp} & \text{if } j_y = i_y \pm 1 \end{cases} \quad (2.47)$$

Here, $i$ and $j$ label the positions of atomic lattice sites in two dimensions, with coordinates $(i_x, i_y)$ and $(j_x, j_y)$, respectively. The case $i = j$ represents the on-site term. The terms $j_x = i_x \pm 1$ and $j_y = i_y \pm 1$ correspond to nearest-neighbour hopping along the $x$- and $y$-directions, respectively as shown in (b) of Fig. 2.4. The hopping parameters $t_{\parallel}$ and $t_{\perp}$ represent nearest-neighbour hopping amplitudes in the tight-binding model. Specifically, $t_{\parallel}$ denotes hopping along the direction of orbital alignment, typically the stronger hopping channel, and $t_{\perp}$ denotes hopping perpendicular to the orbital alignment, generally weaker due to reduced orbital overlap.

To visualize this, we include the schematic representation of $d_{xy}$ orbitals and their nearest-neighbour hopping pathways in Fig.2.4. To proceed further, we explicitly evaluate how each hopping contribution—from on-site and nearest-neighbour interactions—affects the diagonal elements of the tight-binding Hamiltonian in momentum space. We now compute these contributions explicitly, starting with the on-site term ($i = j$) and then evaluating the

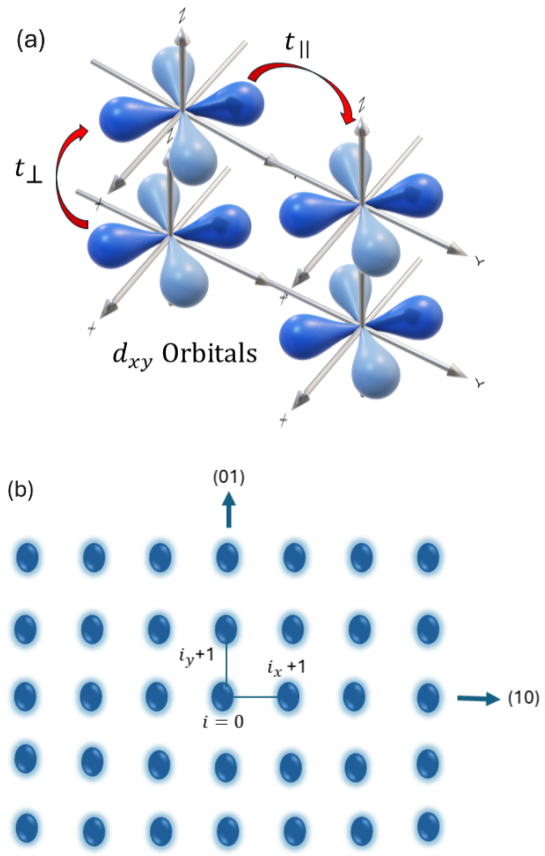


Figure 2.4: (a) Nearest-neighbor hopping for $d_{xy}$ orbitals, with $t_{||}$ and $t_{\perp}$ denoting hopping directions parallel and perpendicular to the orbital lobes. (b) Lattice indexing in the $xy$-plane, showing the central site $(0, 0)$ and its nearest neighbors in the tight-binding grid.

phase factors associated with nearest-neighbour hopping along the $x$- and $y$-directions.

For on-site energy $(i = j)$,

$$e^{i(k_x x_i - k_x x_j + k_y y_i - k_y y_j)} = e^0 = 1, \tag{2.48}$$

For nearest-neighbour hopping,

- When $j_x = i_x + 1$:

$$e^{ik_x(x_i - x_j)} = e^{-ik_x a} \quad \Rightarrow \quad -t_{||} e^{-ik_x a}$$

- When $j_x = i_x - 1$:

$$e^{ik_x(x_i - x_j)} = e^{ik_x a} \quad \Rightarrow \quad -t_{||} e^{ik_x a}$$

- When $j_y = i_y + 1$:

$$e^{ik_y(y_i - y_j)} = e^{-ik_y a} \quad \Rightarrow \quad -t_\perp e^{-ik_y a}$$

- When $j_y = i_y - 1$:

$$e^{ik_y(y_i - y_j)} = e^{ik_y a} \quad \Rightarrow \quad -t_\perp e^{ik_y a}$$

Summing these contributions, we obtain,

$$\epsilon^{xz}_{0,\vec{k}} = t_0 - t_\parallel e^{-ik_x a} - t_\parallel e^{ik_x a} - t_\perp e^{-ik_y a} - t_\perp e^{ik_y a} \tag{2.49}$$

which simplifies using Euler's formula:

$$\epsilon^{xz}_{0,\vec{k}} = t_0 - 2t_\parallel \cos(k_x a) - 2t_\perp \cos(k_y a) \tag{2.50}$$

Similarly, the tight-binding dispersion relations for the $t_{2g}$ orbitals without spin-orbit coupling are given by:

$$\epsilon^{xy}_{0,\vec{k}} = E_{xy} - 2t_\parallel(c_x + c_y) - 4t_{3x} c_x c_y \,, \tag{2.51}$$

$$\epsilon^{yz}_{0,\vec{k}} = E_{yz} - uP_x^2 - 2t_\perp c_x - 2t_\parallel c_y \,, \tag{2.52}$$

$$\epsilon^{zx}_{0,\vec{k}} = E_{zx} - 2t_\parallel c_x - 2t_\perp c_y \,, \tag{2.53}$$

where $E_{xy}$, $E_{yz}$, and $E_{zx}$ are the orbital-specific energy shifts and $c_i = \cos k_i$ for $i = x, y, z$. Among the three on-site energy terms, the expression for $\epsilon^{yz}_{0,\vec{k}}$ includes an additional term proportional to $u(P_x)^2$. This term is allowed by symmetry, as it is invariant under all spatial reflection operations and TRS. We include this term in the TB model to capture polarization-induced shifts in the orbital energies, consistent with the results of DFT calculations. The coefficient $u$ is treated as a fitting parameter to quantitatively match the tight-binding dispersion with the DFT band structure.

## 2.9 All Symmetries Together

Building upon the detailed symmetry analysis performed in the previous section for a specific off-diagonal matrix element, we now apply the same methodology systematically to all relevant hopping terms and on-site energies in the TB Hamiltonian. By considering the transformations under reflections in the $xy$-, $yz$-, and $xz$-planes, as well as TRS, we derive the symmetry-constrained forms of each matrix element. The results of this comprehensive analysis are summarized in the Table 3.2, which provides a unified overview of how each non-zero term behaves under the imposed symmetries.

| **Element** | $\hat{\sigma}_x$ | $\hat{\sigma}_y$ | $\hat{\tau}$ |
|---|---|---|---|
| $t^{yz,zx}_{0,\vec{k}}$ | $-t^{yz,zx}_{0,(-k_x,k_y)}$ | $-t^{yz,zx}_{0,(k_x,-k_y)}$ | $[t^{yz,zx}_{0,-\vec{k}}]^*$ |
| $t^{xy,yz}_{1,\vec{k}}$ | $-t^{xy,yz}_{1,(-k_x,k_y)}$ | $-t^{xy,yz}_{1,(k_x,-k_y)}$ | $[-t^{xy,yz}_{1,-\vec{k}}]^*$ |
| $t^{xy,xz}_{1,\vec{k}}$ | $t^{xy,xz}_{1,(-k_x,k_y)}$ | $t_{1,(k_x,-k_y)}$ | $[-t^{xy,xz}_{1,-\vec{k}}]^*$ |
| $t^{xy,yz}_{2,\vec{k}}$ | $t^{xy,yz}_{2,(-k_x,k_y)}$ | $+t^{xy,yz}_{2,(k_x,-k_y)}$ | $[-t^{xy,yz}_{2,-\vec{k}}]^*$ |
| $t^{xy,xz}_{2,\vec{k}}$ | $-t^{xy,xz}_{2,(-k_x,k_y)}$ | $-t^{xy,xz}_{2,(k_x,-k_y)}$ | $[-t^{xy,xz}_{2,-\vec{k}}]^*$ |
| $t^{yz,xz}_{3,\vec{k}}$ | $t^{yz,xz}_{3,(-k_x,k_y)}$ | $+t^{yz,xz}_{3,(k_x,-k_y)}$ | $[-t^{yz,xz}_{3,-\vec{k}}]^*$ |
| $\epsilon^{\alpha}_{\vec{k}}$ | $\epsilon^{\alpha}_{(-k_x,k_y)}$ | $\epsilon^{\alpha}_{(k_x,-k_y)}$ | $[\epsilon^{\alpha}_{-\vec{k}}]^*$ |

Table 2.2: Symmetry relations for the nonzero matrix elements of $H_{\mu,\vec{k}}$. Each row shows terms that must be equal due to symmetry operations: reflection in $x$ which flips polarization ($P_x \to -P_x$), reflection in $y$, and time-reversal symmetry. Hermiticity ensures that diagonal terms $\epsilon^{\alpha}_{\vec{k}}$ are real.

Repeating the symmetry analysis for the remaining parts of Eq. (2.16), we obtain

$$H_{1,\vec{k}} = \begin{pmatrix} 0 & it^{xy,yz}_{11}s_xs_y + t^{xy,yz}_{12}s_yP_x & -i\frac{\xi}{2} + t^{xy,xz}_{12}s_xP_x \\ -it^{xy,yz}_{11}s_xs_y + t^{xy,yz}_{12}s_yP_x & 0 & 0 \\ i\frac{\xi}{2} + t^{xy,xz}_{12}s_xP_x & 0 & 0 \end{pmatrix}. \quad (2.54)$$

The terms proportional to $\xi/2$ in the matrix represent the ASOC, as introduced earlier in Chapter 1. Here, $\xi$ denotes the spin–orbit coupling strength, which for titanium is approximately $\xi \approx 20$ meV. Notably, this contribution arises independently of the ferroelectric polarization.

Similarly, for $H_{2,\vec{k}}$, we write,

$$H_{2,\vec{k}} = \begin{pmatrix} 0 & t_{22}^{xy,yz} s_x P_x + i\frac{\xi}{2} & t_{22}^{xy,xz} s_y P_x + i t_{21}^{xy,xz} s_x s_y \\ t_{22}^{xy,yz} s_x P_x - i\frac{\xi}{2} & 0 & 0 \\ t_{22}^{xy,xz} s_y P_x - i t_{21}^{xy,xz} s_x s_y & 0 & 0 \end{pmatrix}. \tag{2.55}$$

For the final term, $H_{3,\vec{k}}$, we have,

$$H_{3,\vec{k}} = \begin{pmatrix} 0 & 0 & 0 \\ 0 & 0 & i\frac{\xi}{2} + t_{32}^{yz,zx} s_x P_x \\ 0 & -i\frac{\xi}{2} + t_{32}^{yz,zx} s_x P_x & 0 \end{pmatrix}. \tag{2.56}$$

Now that we have systematically constructed the components of the total Hamiltonian by identifying and retaining only those terms that are invariant under the relevant symmetries, including reflections across the coordinate planes and time-reversal symmetry, we have arrived at compact expressions for each sub-block, $\mathbf{H}_{1,\vec{k}}$, $\mathbf{H}_{2,\vec{k}}$, and $\mathbf{H}_{3,\vec{k}}$. With the full TB Hamiltonian now assembled from these symmetry-constrained components, we are in a position to proceed with the numerical analysis. In the following chapter, we will use these Hamiltonian matrices to compute the band structures of the system under various polarization conditions. This will allow us to explore the resulting energy dispersions, identify the nature of the band splitting due to spin-orbit interaction and ferroelectric polarization,

and evaluate the overall impact of symmetry breaking on the electronic properties of the system.

# Chapter 3

# Results & Discussions

## 3.1 Overview and Research Objectives

In the introduction, we highlighted the central questions guiding this work:

> *How does ferroelectric polarization influence the energy dispersion of conduction bands at charged domain walls in $BaTiO_3$?*
>
> *How do symmetry constraints imposed by polarization shape the spin texture of the two-dimensional electron gas?*

To explore these questions, we formulated several specific objectives:

1. Investigate the role of crystalline symmetry on the Hamiltonian of $BaTiO_3$ in the tetragonal phase with polarization across a 90° head-to-head domain wall. We analyzed how the symmetry constraints dictated the allowed hopping terms and affect the orbital degeneracies.

2. Determine how the inclusion of ASOC modifies the band structure. We will assess the extent to which ASOC lifts degeneracies and generates spin splittings.

3. Examine how introducing ferroelectric polarization further alters the electronic states. Specifically, we will quantify how polarization-induced inversion symmetry breaking modifies the band dispersion and the Fermi surface topology.

4. Analyze the role of additional spin-orbit terms that arise due to structural asymmetry. We will investigate how these terms couple the spin and momentum degrees of freedom, leading to momentum-dependent spin textures and Ising-type spin splitting.

5. Discuss the broader implications of these findings. We will consider how the emergence of nontrivial spin textures and tunable spin splittings in ferroelectric $BaTiO_3$ could be harnessed for reconfigurable spintronic applications.

## 3.2 Modeling Approach and Justification

To capture these effects, the study considers three progressive scenarios, (i) the unpolarized system without SOC, serving as a reference configuration; (ii) the inclusion of ASOC while preserving inversion symmetry; and (iii) the full model incorporating both SOC and inversion symmetry breaking terms. This stepwise approach enables a clear separation of the contributions from each interaction and provides insights into their combined influence on the electronic structure. All calculations are performed along high-symmetry directions in the Brillouin zone, and complementary Fermi surface contours are constructed to illustrate the changes in the topology of occupied states.

## 3.3 Computational Details and Band Structure Fitting

To investigate the low-energy electronic structure of $BaTiO_3$, we performed the density functional theory (DFT) calculations and then constructed a quantitative TB model by fitting its parameters to the DFT results. These calculations were performed by Dr. Bill Atkinson using Quantum ESPRESSO [44, 45]. Fully-relativistic, norm-conserving Vanderbilt pseudopotentials [46] were used, with a plane-wave energy cutoff of 60 Ry.

The calculations were carried out for tetragonal $BaTiO_3$ with lattice constants $a = b = 4.00$ Å, $c = 4.03$ Å. The atomic positions, in fractional units of the lattice constants, were adopted from Ref. [47] and are listed below:

| **Atom** | $x$ | $y$ | $z$ |
|---|---|---|---|
| Ba | 0.000 | 0.000 | 0.000 |
| Ti | 0.500 | 0.500 | 0.518 |
| O1 | 0.500 | 0.000 | 0.475 |
| O2 | 0.000 | 0.500 | 0.475 |
| O3 | 0.500 | 0.500 | −0.0123 |

The self-consistent wavefunctions are solved on on an $8 \times 8 \times 8$ mesh of $k$-points.

From the resulting 3D DFT band structure, we identified the three conduction bands immediately above the Fermi level, which arise predominantly from Ti $t_{2g}$ orbitals ($d_{xy}$, $d_{yz}$, and $d_{zx}$). These form the low-energy basis for our TB model, as described in Chapter 2. To ensure consistency, the TB model was evaluated in three dimensions and fit directly to the DFT band structure to extract key parameters such as orbital energy offsets and hopping amplitudes.

For the diagonal terms, we began with generic $t_{2g}$ orbital dispersions for the $d_{xy}$, $d_{yz}$, and $d_{zx}$ bands in 3D,

$$\epsilon^{xy} = E_{xy} - 2t_{\parallel}(c_x + c_y) - 2t_{\perp}c_z - 4t_{3x}c_x c_y \,, \tag{3.1}$$

$$\epsilon^{yz} = E_{yz} - uP_x^2 - 2t_{\perp}c_x - 2t_{\parallel}c_y - 2t_{\parallel}c_z - 4t_3 c_y c_z \,, \tag{3.2}$$

$$\epsilon^{zx} = E_{zx} - 2t_{\parallel}c_x - 2t_{\perp}c_y - 2t_{\parallel}c_z - 4t_{3x}c_z c_x \,, \tag{3.3}$$

The parameters obtained from this fitting process are:

$$E_{xy} = 15.2992 \text{ eV}, \quad E_{yz} = 14.6744 \text{ eV}, \quad E_{zx} = 14.6265 \text{ eV},$$
$$t_{\parallel} = 0.2361 \text{ eV}, \quad t_{\perp} = 0.0367 \text{ eV}, \quad t_3 = 0.1 \text{ eV}, \quad u = 0.1, \quad t_{3x} = 0.0565 \text{ eV}.$$

To check how well the TB model matches the DFT results, we compare them in Fig. 3.1. The red dots correspond to the TB model results, while the blue dots represent the DFT band structure along selected high-symmetry paths in the Brillouin zone. The TB model matches the shape and placement of the conduction bands very well, especially near the Γ point and along $\Gamma \to X$ and $\Gamma \to Y$. Minor discrepancies at higher energy points are due to neglected higher-order terms and simplifications inherent in the model.

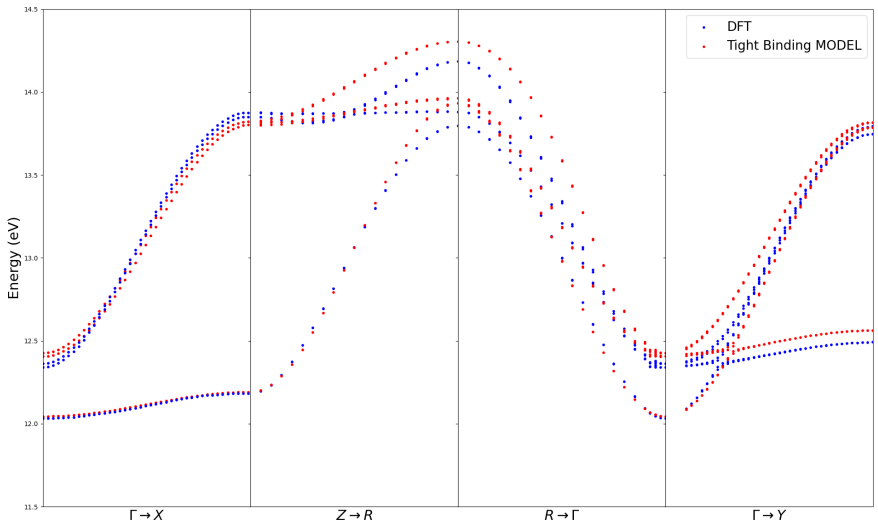


Figure 3.1: Comparison of DFT (blue) and tight-binding model (red) band structures for domain wall in $BaTiO_3$.

Next, we addressed the off-diagonal components of the Hamiltonian that govern orbital mixing and SOC. Initially, our model included nine terms corresponding to symmetry-allowed couplings in the presence of a polarization along the $x$-direction ($P_x$). These terms

are,

$$t_{01}s_xs_y, \quad it_{02}^{yz,zx}s_yP_x, \quad it_{11}^{xy,yz}s_xs_y,$$
$$t_{12}^{xy,yz}s_yP_x, \quad t_{12}^{xy,xz}s_xP_x, \quad t_{22}^{xy,yz}s_xP_x,$$
$$t_{22}^{xy,xz}s_yP_x, \quad it_{21}^{xy,xz}s_xs_y, \quad t_{32}^{yz,zx}s_xP_x.$$

However, some of these terms such as $t_{01}s_xs_y$ have a quantitative effect on the band structure, but do not contribute to the spin-orbit physics. Therefore, these were set to zero, reducing the number of effective unknowns. We will show in Sec.(3.4.2) that terms involving $\sin k_x$ (e.g., $t_{12}^{xy,xz}s_xP_x$) have negligible influence on the spin splitting of the bands near the Fermi level. Therefore, we set these terms to zero at this stage, which reduces the number of effective unknown parameters in the model.

We mainly focus on the role of inversion symmetry breaking and the terms responsible for that are,

$$t_{12}^{xy,yz}s_yP_x, \quad t_{22}^{xy,xz}s_yP_x, \quad it_{02}^{yz,zx}s_yP_x.$$

These terms directly couple the orbital and spin degrees of freedom through the polarization field and are primarily responsible for the emergence of Ising-type spin splitting observed in our calculations.

Table (3.1) summarizes the values assigned to these off-diagonal terms. Only these three were given a finite value of approximately 0.1 eV, chosen after exploring parameter ranges and comparing with DFT results to produce realistic spin splitting. Although this value is relatively large for SOC-related hopping terms, it was intentionally set high to clearly show spin-orbit effects in the band structures and spin textures. All other terms were set to zero due to their minor or negligible effects.

Overall, this TB framework allows us to interpret and reproduce the essential features of the DFT band structure while highlighting the role of polarization-induced orbital mixing and SOC effects.

| Off-diagonal Term | Value |
|---|---|
| $t_{01}s_xs_y$ | 0 |
| $it_{02}^{yz,zx}s_yP_x$ | $0.1eV$ |
| $it_{11}^{xy,yz}s_xs_y$ | 0 |
| $t_{12}^{xy,yz}s_yP_x$ | $0.1eV$ |
| $t_{12}^{xy,xz}s_xP_x$ | 0 |
| $t_{22}^{xy,yz}s_xP_x$ | 0 |
| $t_{22}^{xy,xz}s_yP_x$ | $0.1eV$ |
| $it_{21}^{xy,xz}s_xs_y$ | 0 |
| $t_{32}^{yz,zx}s_xP_x$ | 0 |

Table 3.1: Values assigned to symmetry-allowed off-diagonal terms in the Hamiltonian. Only three contribute significantly to spin splitting.

### 3.3.1 Electron Filling and Fermi Level Determination

To establish the Fermi level corresponding to a physically meaningful electronic filling, the occupancy of each state was computed explicitly by summing the eigenvalues of the Hamiltonian across a discretized two-dimensional $k$-space grid. The Fermi-Dirac distribution at zero temperature is

$$f(E) = \begin{cases} 1, & E < E_F, \\ 0, & E \geq E_F, \end{cases}$$

where $E_F$ denotes the Fermi level. For each $k$-point, the total electron occupation was obtained by summing over all occupied bands,

$$n_{\text{occ}}(k_x, k_y) = \sum_i f\big(E_i(k_x, k_y)\big),$$

where $E_i(k_x, k_y)$ are the eigenvalues of the Hamiltonian computed at each point $(k_x, k_y)$ for the ith band.

The calculation employed a uniform $k$-space mesh defined by

$$k_x, k_y \in \left[-\pi,\, \pi\right],$$

sampled over 200 points in each direction.

The total number of electrons was evaluated by summing the occupancy over all $k$-points,

$$N_{\text{tot}} = \sum_{k_x} \sum_{k_y} n_{\text{occ}}(k_x, k_y).$$

Finally, the average electron occupancy per $k$-point was calculated as

$$\langle n \rangle = \frac{N_{\text{tot}}}{N_k}.$$

Using this procedure, the Fermi level was determined which ensured the filling consistent with the band structure and the assumed two-dimensional electron gas. This Fermi level was subsequently adopted for all band structure and Fermi surface calculations presented in the following sections. The calculated total occupancy of the 2DEG corresponds to an average of approximately 0.3698 electrons per unit cell. Using the relation for the bound charge at a charged domain wall,

$$\sigma_b = 2P \cos\theta, \tag{3.4}$$

where $P = 0.26$ C/m$^2$ for $BaTiO_3$ and $\theta = 45^\circ$, we obtain

$$\sigma_b = 2 \times 0.26 \times \cos(45^\circ) \approx 0.52 \times 0.7071 \approx 0.3677 \text{ C/m}^2. \tag{3.5}$$

Considering the tetragonal lattice parameters of $BaTiO_3$, $a = 4.0$ Å and $c = 4.03$ Å, the area of the unit cell perpendicular to the domain wall is

$$A_{\text{uc}} = a \times c = (4.0 \times 10^{-10}) \times (4.03 \times 10^{-10}) \approx 1.612 \times 10^{-19} \text{ m}^2. \tag{3.6}$$

The corresponding number of electrons per unit cell is then

$$n_e = \frac{\sigma_b \times A_{\text{uc}}}{e} = \frac{0.3677 \times 1.612 \times 10^{-19}}{1.602 \times 10^{-19}} \approx 0.369 \text{ electrons per unit cell.} \tag{3.7}$$

## 3.4 Domain Wall Band Structures for $H_0$

Now that we have determined all relevant parameters for our TB model including both diagonal and off-diagonal terms, we are well positioned to compute and analyze the resulting band structures for our 2D model. This allows us to visualize how the orbital and symmetry properties shape the low-energy electronic landscape of $BaTiO_3$, starting with the baseline case that excludes SOC and polarization effects. Fig. 3.2 shows the electronic band structure of $BaTiO_3$ obtained from the spin-independent TB Hamiltonian $H_0$. This represents the reference configuration with no ferroelectric polarization and no SOC.

At the $\Gamma$ point ($\vec{k} = 0, 0$), the three lowest conduction bands are nearly degenerate. However, as we move along the $\Gamma \rightarrow X$ direction ($\vec{k} = (\pi, 0)$), this degeneracy is lifted. Two of the bands—mainly from the $d_{xy}$ and $d_{zx}$ orbitals—rise in energy, while the third band, associated with the $d_{yz}$ orbital, stays relatively flat.

This difference comes from how each orbital allows electrons to hop along the $x$-direction. The $d_{xy}$ and $d_{zx}$ orbitals support strong hopping in this direction, with a large hopping value of $t_{\parallel} = 236$ meV. On the other hand, the $d_{yz}$ orbital doesn't contribute much to hopping along $x$, and its energy varies mainly due to the much smaller perpendicular hopping term, $t_{\perp} = 36$ meV. This explains why the $d_{yz}$ band shows little dispersion, while the other two rise more noticeably as we move from $\Gamma$ to $X$.

Along the $X \rightarrow M[\vec{k} = (\pi, \pi)]$ path, all three bands continue to disperse. The upper band exhibits a clear peak, while the lower bands remain less dispersive. Near the $M$ point, a direct crossing between the lower and middle bands becomes visible. This band structure serves as a benchmark for identifying how inversion symmetry breaking alters the band structure in subsequent sections. The horizontal dashed line denotes the Fermi level determined as described in the preceding section, which serves as the energy reference for the occupied states and defines the cut used to compute the corresponding Fermi surface.

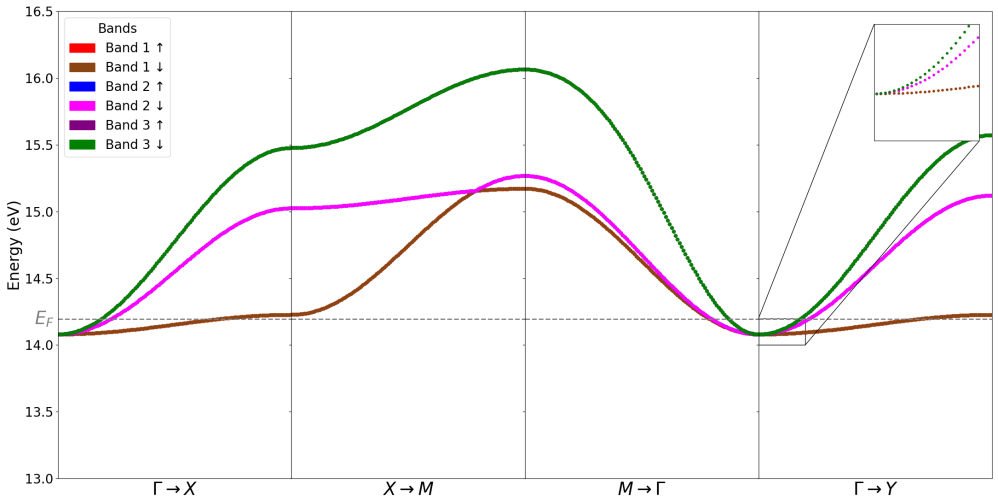


Figure 3.2: Band structure for the domain wall in $BaTiO_3$ without polarization

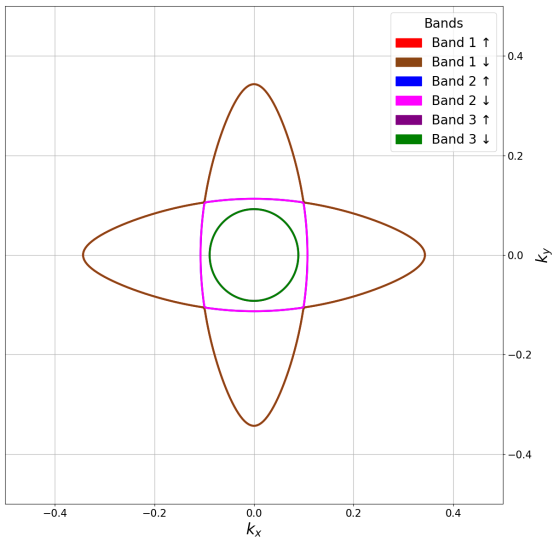


Figure 3.3: Domain wall Fermi surface without polarization

Figure 3.3 shows the computed Fermi surface of $BaTiO_3$ in the absence of SOC and inversion symmetry breaking, corresponding to the reference Hamiltonian $H_0$. The Fermi surface consists of three distinct, closed lines associated with the $t_{2g}$ orbitals. Each line is spin-degenerate and exhibits the high symmetry characteristic. This simple case provides a

clear point of comparison for later cases, where SOC and ferroelectric polarization introduce distortions and splittings. In this configuration, the undisturbed Fermi surface defines the baseline charge transport properties of $BaTiO_3$ in its paraelectric state.

### 3.4.1 Inclusion of Atomic Spin-Orbit Coupling

Including ASOC modifies the band dispersion in several important ways. Figure 3.4 shows that ASOC lifts some degeneracies by coupling the spin and orbital degrees of freedom, leading to avoided crossings where bands previously intersected. A representative avoided crossing is highlighted in the inset of Fig. 3.4, where a gap opens as a direct manifestation of spin-orbital mixing. Compared to Fig. 3.2, this band structure displays clear splitting induced by ASOC, while the overall dispersions remain largely unchanged away from the crossing points. The corresponding Fermi surface is shown in Fig. 3.5. The contours are slightly shifted and deformed due to the influence of ASOC. Despite the inclusion of ASOC terms, there is no spin splitting of the bands, indicating that additional symmetry breaking is required to lift the spin degeneracy in $BaTiO_3$.

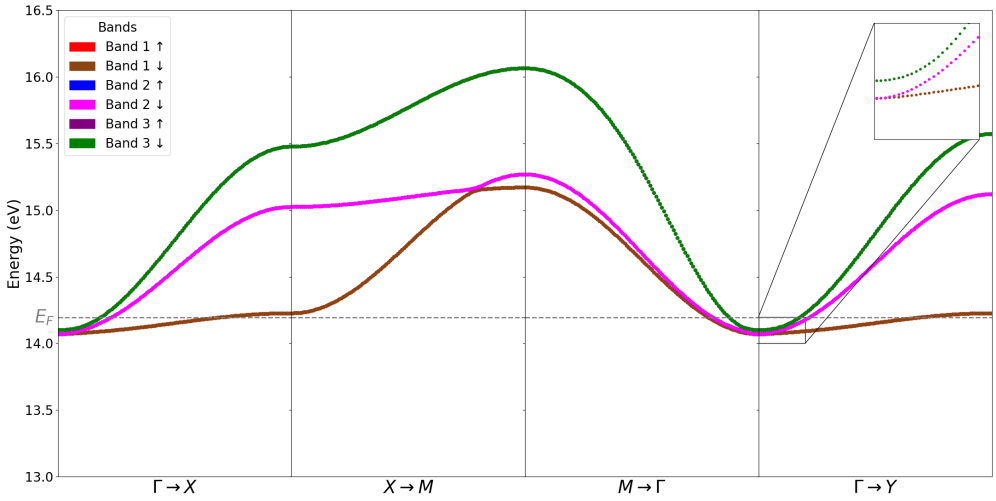


Figure 3.4: Electronic band structure for the domain wall including ASOC effects.

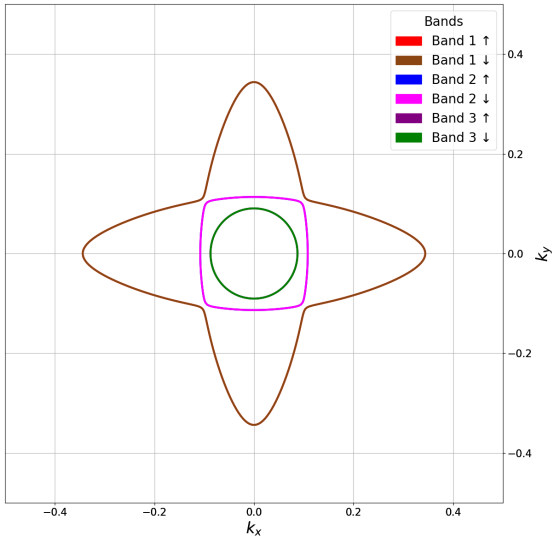


Figure 3.5: Fermi Surface for the domain wall including ASOC effects.

### 3.4.2 Full Hamiltonian with All Couplings

Figure 3.6 shows the domain wall band structure computed with the full tight-binding Hamiltonian, including inversion symmetry breaking due to polarization ($P_x$) and SOC. Along the $\Gamma \to X$ path, we observe no visible spin splitting between the bands. This is consistent with the symmetry of the system. Since $k_y = 0$ along this direction, all terms in the Hamiltonian that involve $\sin k_y$ , including the orbital-mixing terms responsible for spin splitting vanish identically. As a result, the bands retain their spin degeneracy.

Along the $X \to M$ path, where both $k_x$ and $k_y$ are nonzero, the $\sin k_y$ terms become active. This leads to pronounced spin splitting. Orbital mixing terms are enhanced in this region, lifting degeneracies and modifying the effective mass of each band.

Along the $\Gamma \to Y$ direction, $k_y$ increases while $k_x = 0$, thereby activating all symmetry-allowed terms in the Hamiltonian that contain $\sin k_y$. Notably, this includes the orbital-mixing terms such as $t_{12}^{xy,yz} s_y P_x$, $t_{22}^{xy,xz} s_y P_x$, and $i t_{02}^{yz,zx} s_y P_x$. We observe a clear spin splitting in this region, where the initially threefold conduction band manifold splits into six distinct bands. Each orbital branch now hosts two spin-polarized components — spin-up and spin-down. Compared to Fig. 3.2, this configuration represents the most pronounced

departure from the reference case, with the original parabolic bands transformed into a complex manifold of non-degenerate branches. Fig. 3.7 shows the Fermi surface obtained using the full TB Hamiltonian. In this case, each band splits into a pair of spin-polarized branches, resulting in six clearly separated Fermi contours. This doubling signals the emergence of spin splitting due to broken inversion symmetry. Moreover, the contours are no longer symmetric, the $k_y$-axis exhibits noticeable stretching compared to the $k_x$ direction. This anisotropy arises from an additional term $uP_x^2$ in the Hamiltonian, which selectively shifts the energy of the $d_{yz}$ orbital and enhances its dispersion along $k_y$.

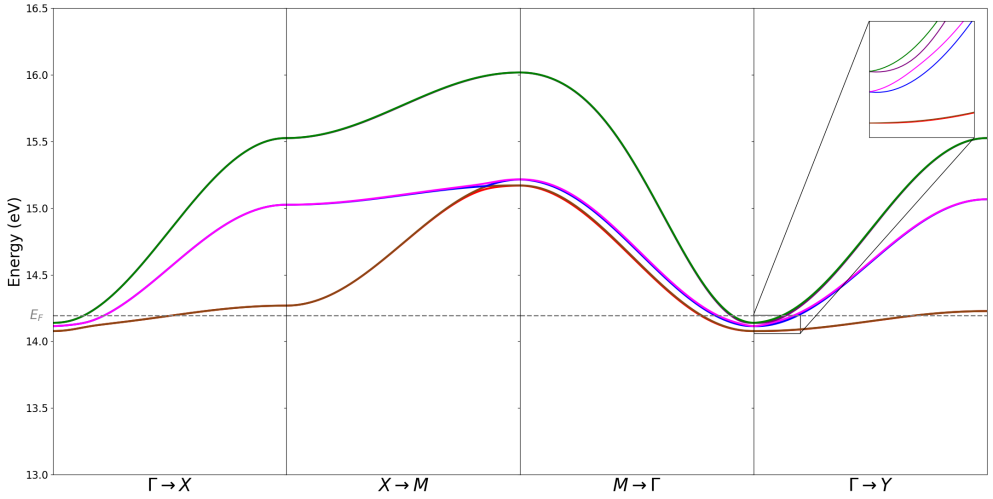


Figure 3.6: Domain wall Hamiltonian with ASOC and SOC

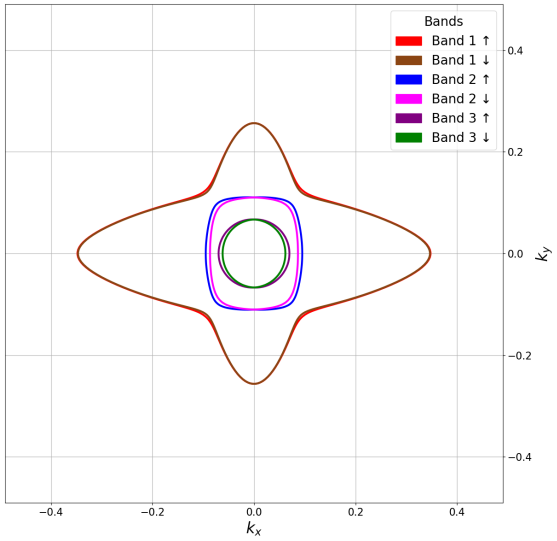


Figure 3.7: Domain wall Fermi surface with ASOC and SOC

During the curve fitting of our model to the DFT band structure, we found that certain symmetry-allowed terms of the form $\sin k_x P_x$, terms that depend on $\sin k_x$, had negligible influence on the electronic bands . To validate this observation, we explicitly included these terms at a representative energy scale of 0.1 eV and recalculated the band structures.
The three plots shown in Fig. 3.8 illustrate the spin splittings obtained by selectively activating subsets of these terms. Spin splitting refers to the lifting of spin degeneracy in the electronic band structure, such that each originally spin-degenerate band separates into two branches (spin-up and spin-down). It is quantified by the energy difference

$$\Delta E_n(\vec{k}) = E_{n,\uparrow}(\vec{k}) - E_{n,\downarrow}(\vec{k}), \tag{3.8}$$

for a given band $n$ and momentum $\vec{k}$.

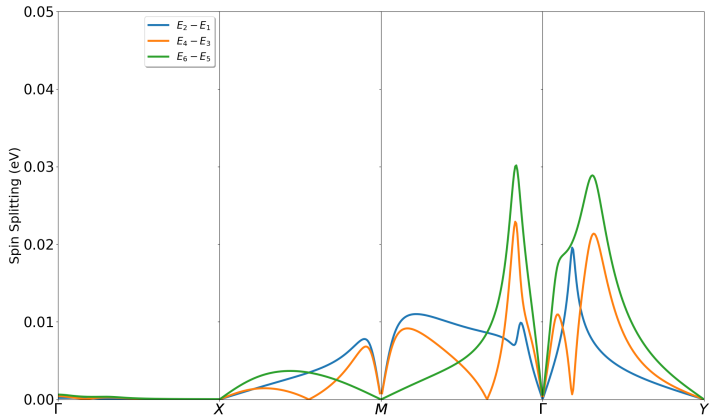


(a) Both $\sin k_x$ and $\sin k_y$ terms active

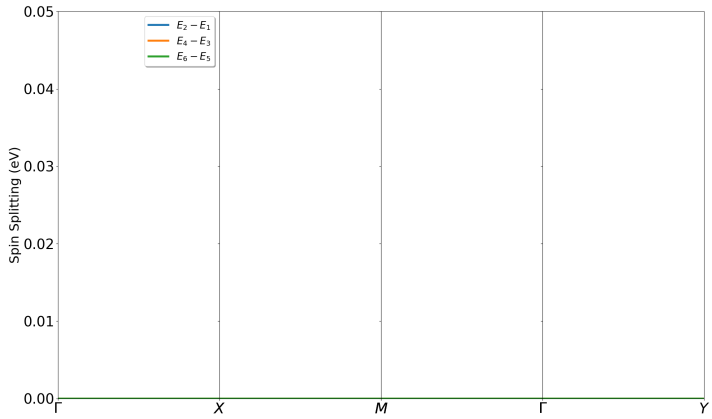


(b) Only $\sin k_x P_x$ terms active

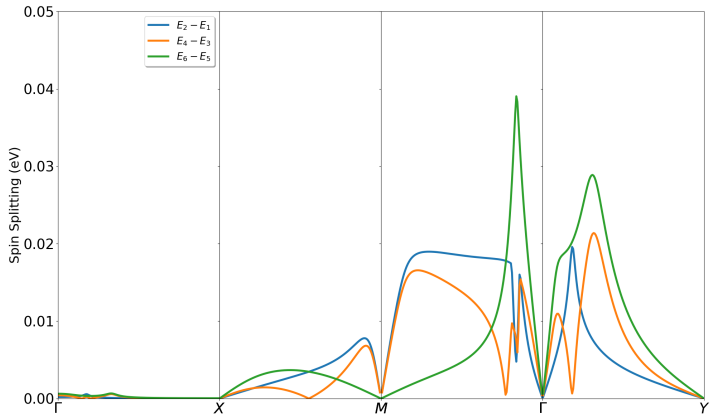


(c) Only $\sin k_y P_x$ terms active

Figure 3.8: Momentum-dependent spin splittings under different subsets of symmetry-allowed off-diagonal terms. (a) includes all $\sin k_x$ and $\sin k_y$ terms; (b) isolates $\sin k_x P_x$ terms, which show negligible splitting; and (c) shows strong splitting driven by $\sin k_y P_x$ terms.

The first panel includes all terms involving both $\sin k_x$ and $\sin k_y$, while the second and third isolate the terms with only $\sin k_x P_x$ and $\sin k_y P_x$ dependence, respectively. A clear pattern emerges: the spin splittings arise from terms proportional to $\sin k_y P_x$, such as $t_{12}^{xy,yz} s_y P_x$, $t_{22}^{xy,xz} s_y P_x$, and $i t_{02}^{yz,zx} s_y P_x$.

Conversely, terms with $\sin k_x P_x$ dependence, simply do not produce spin splitting at all as seen in the second panel.

These results demonstrate that the symmetry and momentum structure of the off-diagonal Hamiltonian terms play a very important role in determining the spin splitting.

## 3.5 Orbital Character

Figure 3.9 presents the orbital-resolved Fermi surfaces of $BaTiO_3$ under ferroelectric polarization. The six panels correspond to the six low-energy bands, with color indicating the dominant $t_{2g}$ orbital character: red for $d_{xy}$, green for $d_{yz}$, and blue for $d_{zx}$. Black contours denote the Fermi level, outlining the momentum-space regions where each band intersects it.

In Bands 1 and 2, the Fermi surfaces are predominantly in green and blue regions, indicating dominant $d_{yz}$ and $d_{zx}$ character—but the boundary between these orbital regions is visibly blurred, especially near the center of the Brillouin zone. This smooth gradient reflects orbital hybridization, a result of symmetry breaking caused by polarization. Bands 3 and 4 continue this trend with a more pronounced mixing. Although they have mostly $d_{yz}$ and $d_{zx}$ character, a distinct red patch appears at the $\Gamma$ point, revealing a localized admixture of $d_{xy}$ character.

In contrast, Bands 5 and 6 exhibit primarily red orbital weight, consistent with $d_{xy}$-dominated states. However, subtle patches of green and blue near the Fermi level crossings indicate that even these bands are not purely $d_{xy}$ in character. This progressive blending of orbital contributions across all bands reflects how ferroelectric polarization drives momentum-dependent orbital mixing.

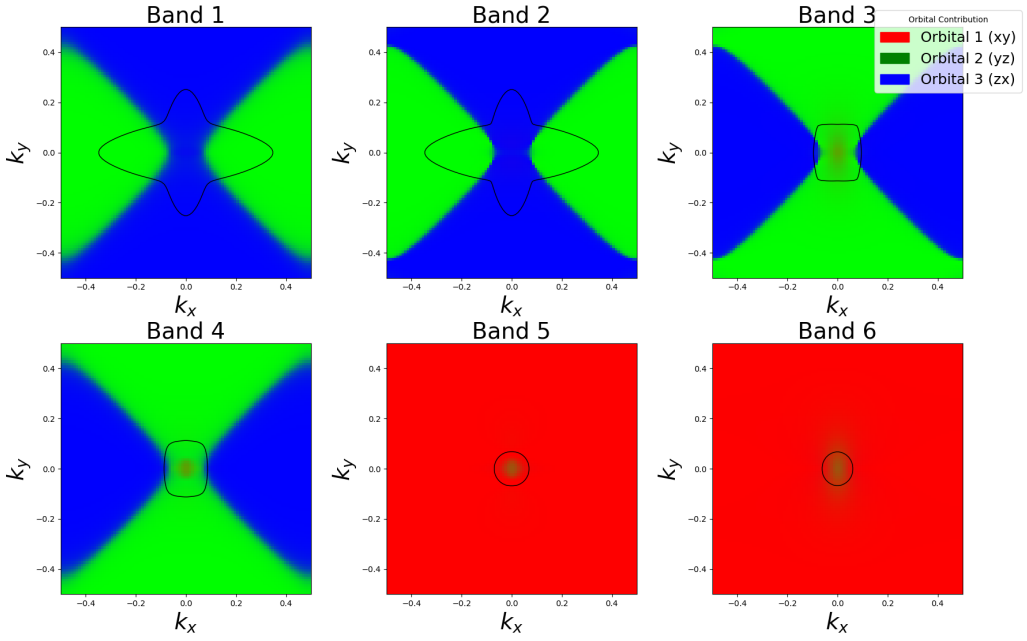


Figure 3.9: Orbital-resolved Fermi surfaces for domain wall with spin-orbit coupling and polarization. Colors indicate dominant orbital character ($d_{xy}$: red, $d_{yz}$: green, $d_{zx}$: blue); black contours mark the Fermi surface for each band.

## 3.6 Spin Expectation Value Calculation

To study the emergence of spin textures at charged 90° domain walls in ferroelectric $BaTiO_3$, we compute the expectation values of the spin operators for each eigenstate of the Hamiltonian. For a given momentum point $\vec{k} = (k_x, k_y)$, the Hamiltonian is diagonalized to yield eigenvalues $\epsilon_n(\vec{k})$ and corresponding eigenvectors $\psi_n(\vec{k})$, where $n$ indexes the band. The spin expectation value $\langle \vec{S} \rangle_n(\vec{k})$ for band $n$ at wavevector $\vec{k}$ is given by,

$$\langle \vec{S} \rangle_n(\vec{k}) = \psi_n^\dagger(\vec{k})\, \vec{\hat{S}}\, \psi_n(\vec{k}), \tag{3.9}$$

where $\vec{\hat{S}} = (\hat{S}_x, \hat{S}_y, \hat{S}_z)$ are the spin operators acting on the spin degree of freedom within each orbital subspace. These spin operators are constructed from the Pauli matrices $\tau_x, \tau_y, \tau_z$, which act on the spin index and are embedded as block-diagonal matrices in the full spin-orbital basis.

For a tight-binding Hamiltonian with spinor wavefunctions of dimension $2N$ (where $N$ is

the number of orbitals), the spin operators are represented as,

$$\hat{S}_x = \frac{\hbar}{2}\begin{bmatrix} 0 & 1 \\ 1 & 0 \end{bmatrix}, \quad \hat{S}_y = \frac{\hbar}{2}\begin{bmatrix} 0 & -i \\ i & 0 \end{bmatrix}, \quad \hat{S}_z = \frac{\hbar}{2}\begin{bmatrix} 1 & 0 \\ 0 & -1 \end{bmatrix},$$

where each matrix is understood to be embedded across the spin degree of freedom for each orbital (e.g., using Kronecker products).

In numerical implementation, the spin expectation values are evaluated using the computed eigenvectors from diagonalizing the Hamiltonian. For each band $n$ and momentum $\vec{k}$, we compute,

$$\langle S_\alpha \rangle_n(\vec{k}) = \sum_{i,j=1}^{2N} \psi^*_{n,i}(\vec{k}) \left[\hat{S}_\alpha\right]_{ij} \psi_{n,j}(\vec{k}), \quad \alpha = x, y, z. \tag{3.10}$$

These spin expectation values are then visualized to reveal the spin textures in momentum space. In our results, we found that $\langle S_x \rangle$ and $\langle S_y \rangle$ vanish due to symmetry, while only $\langle S_z \rangle$ remains finite. This is a hallmark of Ising-type SOC, where the spin is pinned along a single direction—in this case, the out-of-plane $z$-axis.

Fig. 3.10 illustrates the out-of-plane spin polarization on the Fermi surface for the charged domain wall configuration. The color scale represents the magnitude and direction of spin: red indicates spin-up, and blue indicates spin-down. The figure compares the spin textures in two cases, with SOC and without SOC. In the absence of SOC (a), the spin-degenerate Fermi surfaces for spin-up and spin-down states exactly overlap across momentum space, resulting in no visible splitting. This overlap demonstrates that the system retains full spin degeneracy in the absence of symmetry-breaking spin-orbit interactions.

In contrast, Fig. 3.10(b) shows the situation with SOC included. Here, red and blue contours indicate the $z$-component of the spin polarization $\langle S_z \rangle$, corresponding to spin-up and spin-down states, respectively. While much of the Fermi surface still exhibits near-degenerate spin states — evident from overlapping red and blue contours — certain regions display significant separation. These points of divergence occur near avoided crossings of different Fermi surface branches, where spin-orbit coupling becomes most active.

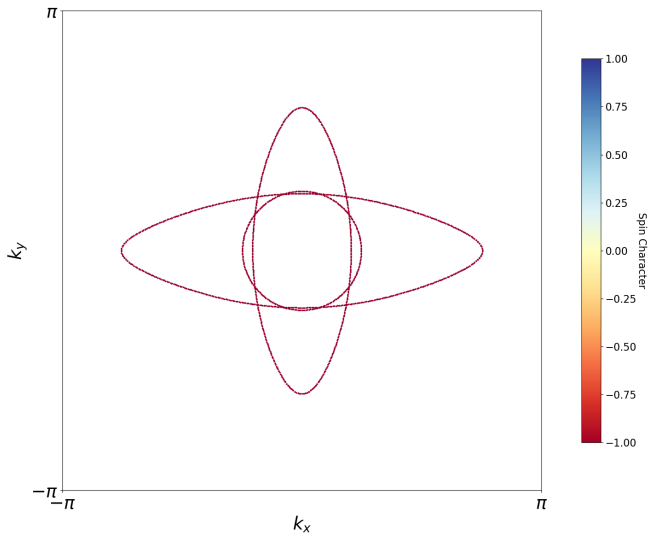


(a)

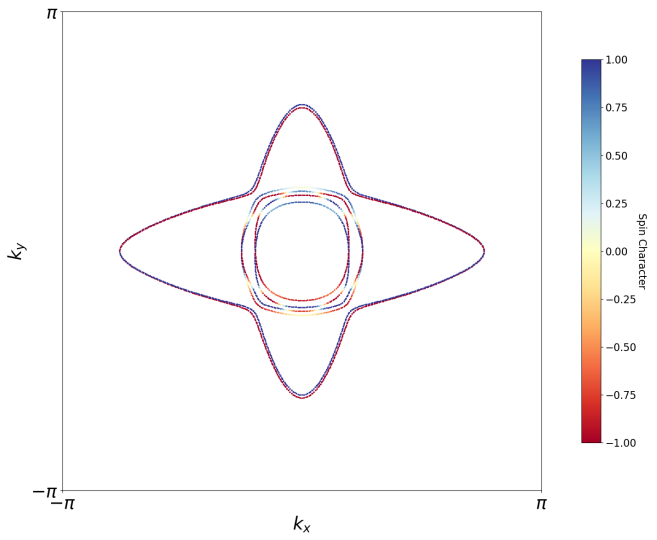


(b)

Figure 3.10: Comparison of spin polarization at the Fermi surface at the CDW in $BaTiO_3$, with and without SOC. (a) Without SOC, the Fermi surfaces cross directly without lifting spin degeneracy, resulting in no spin splitting or avoided crossings. (b)With SOC significant spin splitting is observed near avoided crossings, where the Fermi surface splits into spin-up (red) and spin-down (blue) contours. This indicates strong momentum-dependent spin-orbit effects.

## 3.7 Current-Induced Spin Polarization and Edelstein Effect

The presence of Ising SOC not only affects the ground-state electronic structure but also leads to observable consequences under nonequilibrium conditions. In particular, the momentum-locked spin texture enables the *Edelstein effect*—a mechanism by which a DC electric field induces a uniform spin polarization. When a current is applied parallel to the domain wall, the Fermi surface is shifted in momentum space, leading to an imbalance in the occupied spin states, and consequently, a net spin polarization emerges. As illustrated in Fig. 3.11,

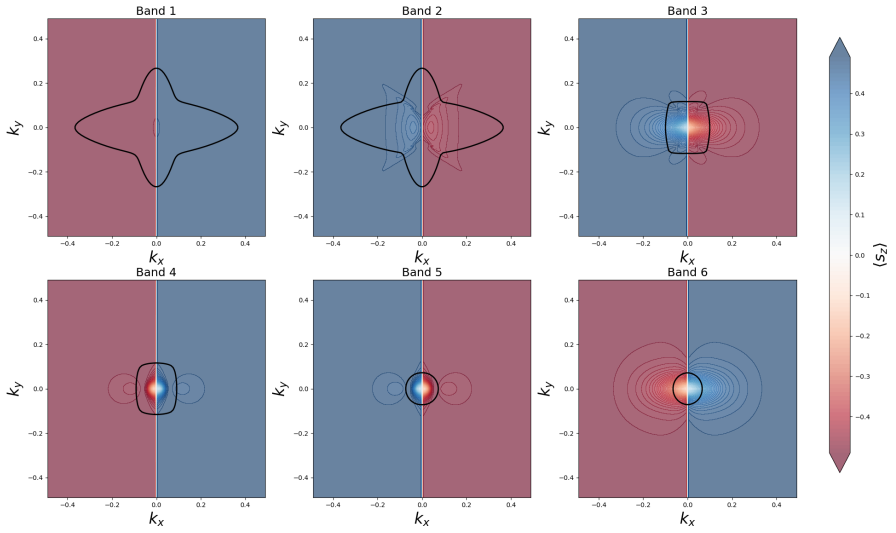


Figure 3.11: Out-of-plane spin expectation values $\langle S_z \rangle$ plotted across the 2D Brillouin zone for all six bands. Each subplot corresponds to one band, with the color scale indicating the magnitude and sign of spin polarization. Red and blue regions indicate spin-up and spin-down components, respectively. The black contours represent the corresponding Fermi surfaces. The coexistence of positive and negative $\langle S_z \rangle$ regions within each band reveals spin splitting, with the Fermi contours highlighting momentum states contributing to current-induced spin polarization.

the Fermi contours for all six bands are superimposed on a colormap representing the out-of-plane spin expectation value $\langle S_z \rangle$.

This electrically induced spin response highlights the potential of such systems for reconfigurable spintronic applications. Because the polarization direction $P_x$ governs the spin-orbit landscape, reversing the ferroelectric polarization allows dynamic tuning of the spin texture. This paves the way for low-power spintronic devices where spin states can be programmed

and erased via gate voltages—key ingredients for non-volatile memory elements and logic devices.

## 3.8 Discussion

The motivation for this work stems from the theoretical framework developed by Zhong *et al.* [48], who investigated SOC at $LaAlO_3/SrTiO_3$ (LAO/STO) interfaces and $SrTiO_3$ (STO) surfaces using DFT calculations combined with a symmetry-constrained TB model. Their study provided critical insights into the orbital origin of Rashba-type SOC in perovskite oxide 2DEGs, emphasizing the role of interface asymmetry and multiorbital effects. Inspired by their approach, our work builds on a similar multiorbital TB framework but shifts the focus from heterointerfaces and surfaces to conducting 90° domain walls. Although both systems share structural similarities—such as the presence of Ti $3d$ $t_{2g}$ orbitals and broken inversion symmetry—the origin and nature of SOC in our system are fundamentally different due to distinct symmetry conditions. One of the most crucial differences lies in the direction of polarization. In the LAO/STO case, inversion symmetry is broken along the out-of-plane direction due to the interface potential gradient, which leads to the emergence of a *Rashba-type SOC* characterized by in-plane spin textures. In contrast, our model for $BaTiO_3$ domain walls assumes that the polarization lies in-plane, consistent with the structure of a head-to-head 90° domain wall. This in-plane polarization changes the symmetry constraints, resulting in a different set of allowed spin–orbital couplings. Notably, we find that under these conditions, the dominant SOC is *Ising-like*, with spin predominantly polarized in the out-of-plane ($z$) direction and locked to in-plane momentum.

While Zhong *et al.* derive their TB parameters directly from DFT and include a well-defined antisymmetric hopping term ($\gamma$) to model interface inversion breaking, our study encountered several unknown coupling terms in the Hamiltonian due to the lack of prior data specific to domain walls in $BaTiO_3$. To overcome this, we used a combination of DFT band structure calculations and curve fitting to estimate a subset of the most influential terms. Given the large number of undetermined parameters, not all terms could be obtained with

high accuracy. Nonetheless, by systematically exploring their effect on the band structure, we were able to isolate the couplings most responsible for band splitting and spin texture formation.

Our results highlight that symmetry and polarization direction are decisive factors in determining the type of SOC. By comparing the interface-induced Rashba splitting observed in LAO/STO to the Ising-type SOC at domain walls in $BaTiO_3$, our study demonstrates that ferroelectric domain walls can serve as a novel platform for achieving spin-polarized electronic states without the need for externally engineered interfaces. Despite being a theoretical result, the prediction of Ising-type SOC at 90° CDWs holds significant potential for future spintronic technologies. The inherent out-of-plane spin polarization and momentum locking—arising purely from symmetry breaking and orbital structure—could be harnessed in designing reconfigurable spin filters, nonvolatile memory elements, or domain-wall-based logic devices [26].

## 3.9 Barriers to Device Integration of Conducting Domain Walls

While our theoretical model shows exciting potential for reconfigurable spintronic devices based on CDWs, turning this idea into a working device still faces a few important challenges.

The first major challenge is the controlled creation and stability of these walls. CDWs are not naturally stable. They need to be screened by mobile electrons, defects, or other mechanisms to avoid building up large internal electric fields [19, 49]. In experiments, forming these walls exactly where and how we want, especially without accidentally forming extra walls nearby, is very difficult. Some studies have tried to solve this by using nano-scale islands or special geometries to confine the domain walls and guide their behavior [50, 51], but this approach is still in early stages.

The second big issue is reading out the wall's signal and integrating it into real devices. Although CDWs can be much more conductive than the surrounding material, the actual current they carry is still very small — often in the nano-ampere range. This makes it

hard to measure them reliably in practical circuits [52]. On top of that, making ferroelectric materials often requires high-temperature processing, which is not compatible with the standard methods used in silicon chip fabrication [53].

Despite these challenges, our model offers a very promising idea. We show that Ising-type SOC can naturally emerge at 90° charged domain walls in tetragonal $BaTiO_3$. This means we can, in principle, control spin orientations and spin–orbit torques just by applying electric fields — without needing any magnetic fields. If researchers can improve the ability to create, stabilize, and read out these domain walls reliably, our model could be the foundation for a new type of low-power, reconfigurable spintronic device that uses both spin and charge.

In short, while it may take time and further experimental work to overcome the remaining barriers, the direction is clear — and the possibilities are very exciting.

# Chapter 4

# Conclusions

This thesis explored the fundamental electronic and spin properties of a 2DEG confined at a 90° head-to-head CDW in tetragonal ferroelectric $BaTiO_3$. Our key question was,

> *What is the effect of polarization on the band structure at a charged domain wall in ferroelectrics?*

Our model is motivated by [48], who investigated SOC at $LaAlO_3/SrTiO_3$ (LAO/STO) interfaces and $SrTiO_3$ (STO) surfaces using DFT calculations combined with a symmetry-constrained TB model. In our study, we focused on understanding the consequences of symmetry breaking, particularly inversion and time-reversal symmetry, on the emergence of SOC phenomena at such nanoscale features.

The symmetries of the system played a crucial role in constraining the form of the Hamiltonian. These constraints enabled a systematic simplification of the orbital-resolved tight-binding Hamiltonian. Particularly, several matrix elements became zero due to symmetry restrictions, reducing the complexity of the model.

We focused on the $t_{2g}$ orbitals ($d_{xy}$, $d_{yz}$, $d_{zx}$), which are known to dominate the conduction band minimum in perovskite oxides. The Hamiltonian we derived included diagonal on-site energy terms and off-diagonal hopping terms. The diagonal terms describe orbital-resolved band energies, while the off-diagonal terms capture orbital mixing arising from inversion symmetry breaking at the domain wall. These orbital mixing terms are the source of SOC

in our model. After constructing the final form of the TB Hamiltonian, we identified several coupling terms whose numerical values for $BaTiO_3$ were not previously reported in the literature. To address this, we performed DFT calculations and compared the resulting band structures with those obtained from our TB model. Using a curve-fitting approach, we extracted approximate values for some of the unknown parameters. However, due to the large number of undetermined terms and the complexity of the model, it was not feasible to determine all values precisely. Instead, we adopted a strategy of estimating reasonable values for selected terms in order to qualitatively explore their influence on the band structure. This allowed us to gain insight into the role of various couplings, particularly those related to spin-orbit interactions and symmetry breaking—in shaping the electronic and spin textures of the system.

The inclusion of SOC had a significant impact on the band structure. In the absence of SOC, the bands exhibited the threefold degeneracy characteristic of bulk $t_{2g}$ orbitals. The introduction of ASOC, primarily helped to lift orbital degeneracies and avoid band crossings. When SOC arising from inversion symmetry breaking at the interface was included, we observed a clear spin splitting of the bands, lifting their degeneracy and resulting in six distinct spin-polarized bands. Together, SOC and ASOC captured the essential physics of spin-split states in low-symmetry environments, consistent with the emergence of momentum-locked spin textures.

One of the most novel findings of this study is the emergence of *Ising-type* spin–orbit coupling at the domain wall. The spin texture analysis revealed that only a single component of spin survives throughout the Brillouin zone, with spins pinned predominantly out of plane. This behavior is a hallmark of Ising type SOC, distinct from conventional Rashba or Dresselhaus types. The result not only highlights a unique physical regime enabled by ferroelectric domain wall engineering but also indicates the potential for robust spin-polarized transport in these systems.

Our results suggest that the momentum-locked spin textures induced by Ising-type SOC could enable phenomena such as the Edelstein effect, where an applied electric field shifts the Fermi surface, resulting in a net spin polarization. This mechanism highlights the potential utility of our findings for spintronic applications, particularly in realizing non-volatile,

low-power devices with electrically reconfigurable spin control.

While our model successfully captures the key physics of spin and orbital behavior near CDWs, it makes a simplification by not explicitly including the finite width of the domain wall. In our approach, we effectively considered only the lowest energy subband (corresponding to the first quantum state, $n = 1$) that arises from confinement across the domain wall. Since the Fermi level lies within this lowest subband, the energy spacing between higher subbands—determined by the width of the domain wall, does not significantly affect the results. However, if the Fermi level were higher and intersected additional subbands (such as $n = 2$ or $n = 3$), the domain wall width would become important, as it controls the separation between these energy levels. Thus, although the domain wall width does not play a major role in our current model, incorporating it will be essential for future studies that aim to explore higher carrier concentrations or more realistic conditions.

Second, the values of the off-diagonal coupling terms used to model orbital mixing were approximate, based on physical intuition and symmetry considerations. While sufficient to demonstrate qualitative effects of SOC, the precise magnitude of these terms remains an open question. More accurate extraction of these couplings can provide deeper insight into the quantitative aspects of spin–orbit engineering.

In conclusion, this thesis presents a powerful model to capture the essence of SOC in ferroelectric domain wall systems. The emergence of Ising-type SOC at CDW in $BaTiO_3$ demonstrates how ferroelectricity and orbital physics can be integrated to engineer novel spin functionalities. As research continues to bridge theoretical modeling with experimental realization, such systems offer a promising platform for future quantum and spintronic technologies.

**Open Questions for Future Research** While this study provides key insights into spin-orbit coupling at charged domain walls, some key research questions remain open for future exploration: How do finite width and wall profile affect spin-orbit coupling (SOC) and spin splitting in these systems? Can inversion-induced SOC parameters be accurately quantified through first-principles Wannier models? What is the actual magnitude of spin polarization when electric fields are applied? Finally, are there other materials or domain wall geometries that might be better suited for achieving robust Ising spin-orbit coupling effects?

# Bibliography


[1] Hikaru Azuma, Shuji Ogata, Ryo Kobayashi, Masayuki Uranagase, Takahiro Tsuzuki, Dilshod Durdiev, and Frank Wendler. Microscopic structure and migration of 90° ferroelectric domain wall in $BaTiO_3$ determined via molecular dynamics simulations. *Journal of Applied Physics*, 133(10), 2023.

[2] R. E. Cohen. Origin of ferroelectricity in perovskite oxides. *Nature*, 358(6382):136–138, 1992.

[3] Malcolm E Lines and Alastair M Glass. *Principles and applications of ferroelectrics and related materials*. Oxford university press, 2001.

[4] Karin M Rabe, Charles H Ahn, and Jean-Marc Triscone. *Physics of ferroelectrics: a modern perspective*, volume 105. Springer Science & Business Media, 2007.

[5] Orlando Auciello, James F Scott, and Ramamoorthy Ramesh. The physics of ferroelectric memories. *Physics today*, 51(7):22–27, 1998.

[6] Ronald CG Naber, Kamal Asadi, Paul WM Blom, Dago M De Leeuw, and Bert De Boer. Organic nonvolatile memory devices based on ferroelectricity. *Advanced materials*, 22(9):933–945, 2010.

[7] An Quan Jiang, Can Wang, Kui Juan Jin, Xiao Bing Liu, James F Scott, Cheol Seong Hwang, Ting Ao Tang, Hui Bin Lu, and Guo Zhen Yang. A resistive memory in semiconducting $BiFeO_3$ thin-film capacitors. *Advanced Materials*, 23(10):1277–1281, 2011.

[8] Dana Georgeta Popescu, Marius Adrian Husanu, Procopios Christou Constantinou, Lucian Dragos Filip, Lucian Trupina, Cristina Ioana Bucur, Iuliana Pasuk, Cristina Chirila, Luminita Mirela Hrib, Viorica Stancu, et al. Experimental band structure of Pb(Zr,Ti)o$_3$ mechanism of ferroelectric stabilization. *Advanced Science*, 10(6):2205476, 2023.

[9] Tianyu Li, Shiqing Deng, Hui Liu, Shengdong Sun, Hao Li, Shuxian Hu, Shi Liu, Xianran Xing, and Jun Chen. Strong room-temperature ferroelectricity in strained srtio$_3$ homoepitaxial film. *Advanced Materials*, 33(21):2008316, 2021.

[10] Aleksandar Radojković, Danijela Luković-Golić, Nataša Jović Orsini, Nenad Nikolić, Jovana Ćirković, Slavica Lazarević, and Željko Despotović. Evolution of ferroelectric and piezoelectric properties of $BiFeO_3$ ceramics doped with lanthanum and zirconium. *Journal of Alloys and Compounds*, 1009:176901, 2024.

[11] A Von Hippel, RG Breckenridge, FG Chesley, and Laszlo Tisza. High dielectric constant ceramics. *Industrial & Engineering Chemistry*, 38(11):1097–1109, 1946.

[12] Yuhuan Xu. *Ferroelectric materials and their applications*. Elsevier, 2013.

[13] J. F. Scott. Ferroelectric memories. *Ferroelectrics Review*, 1(1):1–24, 2000.

[14] Pavel Goudochnikov and Andrew J Bell. Correlations between transition temperature, tolerance factor and cohesive energy in2+: 4+ perovskites. *Journal of Physics: Condensed Matter*, 19(17):176201, 2007.

[15] K Muthu and colleagues. Experimental and first-principles investigation of structural, electronic, optical, elastic and ferroelectric properties of $BaTiO_3$. *Physica B: Condensed Matter*, 674:415548, 2024.

[16] Andrzej Koleżyński and Katarzyna Tkacz-Śmiech. From the molecular picture to the band structure of cubic and tetragonal barium titanate. *Ferroelectrics*, 314(1):123–134, 2005.

[17] X Zhang, T Hashimoto, and DC Joy. Electron holographic study of ferroelectric domain walls. *Applied physics letters*, 60(6):784–786, 1992.

[18] Maxim Y Gureev, Alexander K Tagantsev, and Nava Setter. Head-to-head and tail-to-tail 180 domain walls in an isolated ferroelectric. *Physical Review B—Condensed Matter and Materials Physics*, 83(18):184104, 2011.

[19] Tomas Sluka, Alexander K Tagantsev, Pavel Bednyakov, and Nava Setter. Free-electron gas at charged domain walls in insulating $BaTiO_3$. *Nature Communications*, 4:1808, 2013.

[20] Tomas Sluka, Alexander K Tagantsev, Pavel Bednyakov, and Nava Setter. Switching of charged ferroelectric domain walls. *Nature communications*, 3:748, 2012.

[21] Nicholas C Bristowe, Philippe Ghosez, Peter B Littlewood, and Emilio Artacho. The origin of two-dimensional electron gases at oxide interfaces: insights from theory. *Journal of Physics: Condensed Matter*, 26(14):143201, 2014.

[22] WA Atkinson. Evolution of domain structure with electron doping in ferroelectric thin films. *Physical Review B*, 106(13):134102, 2022.

[23] BC Cornell and WA Atkinson. Influence of a realistic multiorbital band structure on conducting domain walls in perovskite ferroelectrics. *Physical Review B*, 108(24):245108, 2023.

[24] Peter Maksymovych, Anna N Morozovska, Pu Yu, Eugene A Eliseev, Ying-Hao Chu, Ramamoorthy Ramesh, Arthur P Baddorf, and Sergei V Kalinin. Tunable metallic conductance in ferroelectric nanodomains. *Nano letters*, 12(1):209–213, 2012.

[25] Linze Li, Jason Britson, Jacob R Jokisaari, Yi Zhang, Carolina Adamo, Alexander Melville, Darrell G Schlom, Long-Qing Chen, and Xiaoqing Pan. Giant resistive switching via control of ferroelectric charged domain walls. 2016.

[26] Jan Seidel, Lane W Martin, Qili He, Q Zhan, Y-H Chu, A Rother, ME Hawkridge, Peter Maksymovych, P Yu, Martin Gajek, et al. Conduction at domain walls in oxide multiferroics. *Nature materials*, 8(3):229–234, 2009.

[27] Petr S Bednyakov and Jiří Hlinka. Charged domain walls in $BaTiO_3$ crystals emerging from superdomain boundaries. *Advanced Electronic Materials*, 9(6):2300005, 2023.

[28] L Feigl, T Sluka, LJ McGilly, A Crassous, CS Sandu, and N Setter. Controlled creation and displacement of charged domain walls in ferroelectric thin films. *Scientific reports*, 6(1):31323, 2016.

[29] Henrik Beccard, Benjamin Kirbus, Elke Beyreuther, Michael Rusing, Petr Bednyakov, Jiri Hlinka, and Lukas M Eng. Nanoscale conductive sheets in ferroelectric $BaTiO_3$: Large hall electron mobilities at head-to-head domain walls. *ACS Applied Nano Materials*, 5(7):8717–8722, 2022.

[30] Petr S Bednyakov, Iegor Rafalovskyi, and Jiří Hlinka. Fragmented charged domain wall below the tetragonal-orthorhombic phase transition in $BaTiO_3$. *Applied Physics Letters*, 126(1), 2025.

[31] Masaki Kato and Masao Ogata. Interatomic spin-orbit coupling in atomic orbital based tight-binding models. *Physical Review B*, 111(3):035137, 2025.

[32] Meng Fang, Xinwei Li, June Sang Lee, Karin M. Rabe, and Xiaoxing Xi. Recent advances in tunable spin-orbit coupling using ferroelectricity. *APL Materials*, 9(6):060704, 2021.

[33] K. V. Shanavas, Z. S. Popović, and S. Satpathy. Theoretical model for rashba spin-orbit interaction in d electrons. *Physical Review B*, 90(16):165108, 2014.

[34] Shuai Ning, Haoliang Liu, Jingxiong Wu, and Feng Luo. Challenges and opportunities for spintronics based on spin orbit torque. *Fundamental Research*, 2(4):535–538, 2022.

[35] Paul Noël, Felix Trier, Luis M Vicente Arche, Julien Bréhin, Diogo C Vaz, Vincent Garcia, Stéphane Fusil, Agnès Barthélémy, Laurent Vila, Manuel Bibes, et al. Non-volatile electric control of spin–charge conversion in a $SrTiO_3$ rashba system. *Nature*, 580(7804):483–486, 2020.

[36] Rahul Mishra and Hyunsoo Yang. Emerging spintronics phenomena and applications. *IEEE Transactions on Magnetics*, 57(1):1–34, 2020.

[37] Nguyen Huynh Duy Khang, Yugo Ueda, and Pham Nam Hai. A conductive topological insulator with large spin hall effect for ultralow power spin-orbit torque switching. *Nature materials*, 17(9):808–813, 2018.

[38] Sasikanth Manipatruni, Dmitri E Nikonov, and Ian A Young. Beyond cmos computing with spin and polarization. *Nature Physics*, 14(4):338–343, 2018.

[39] Gervasi Herranz, Gyanendra Singh, Nicolas Bergeal, Alexis Jouan, Jérôme Lesueur, Jaume Gázquez, María Varela, Mateusz Scigaj, Nico Dix, Florencio Sánchez, et al. Engineering two-dimensional superconductivity and rashba spin-orbit coupling in $LaAlO_3/SrTiO_3$ quantum wells by selective orbital occupancy. *Nature communications*, 6(1):6028, 2015.

[40] Christian R. Ast and Isabella Gierz. sp-band tight-binding model for the bychkov–rashba effect in a two-dimensional electron system including nearest-neighbor contributions from an electric field. *Physical Review B*, 86(8):085105, 2012.

[41] H. Salehi, V. Fallahi, G. Rezaei, and S. M. Elahi. Band structure of tetragonal $BaTiO_3$. *The European Physical Journal B - Condensed Matter and Complex Systems*, 32(2):177–180, March 2003.

[42] Pierre Tolédano, Mael Guennou, and Jens Kreisel. Order-parameter symmetries of domain walls in ferroelectrics and ferroelastics. *Physical Review B*, 89(13):134104, 2014.

[43] Kiyoyuki Terakura and Shoji Ishibashi. Mechanism of covalency-induced electric polarization within the framework of maximally localized wannier orbitals. *Physical Review B*, 91(19):195120, 2015.

[44] Paolo Giannozzi, Stefano Baroni, Nicola Bonini, Matteo Calandra, Roberto Car, Carlo Cavazzoni, Davide Ceresoli, Guido L Chiarotti, Matteo Cococcioni, Ismaila Dabo, et al. Quantum espresso: a modular and open-source software project for quantumsimulations of materials. *Journal of physics: Condensed matter*, 21(39):395502, 2009.

[45] Paolo Giannozzi, Oliviero Andreussi, Thomas Brumme, Oana Bunau, M Buongiorno Nardelli, Matteo Calandra, Roberto Car, Carlo Cavazzoni, Davide Ceresoli, Matteo Cococcioni, et al. Advanced capabilities for materials modelling with quantum espresso. *Journal of physics: Condensed matter*, 29(46):465901, 2017.

[46] DR Hamann. Erratum: optimized norm-conserving vanderbilt pseudopotentials [phys. rev. b 88, 085117 (2013)]. *Physical Review B*, 95(23):239906, 2017.

[47] ES Goh, LH Ong, TL Yoon, and KH Chew. Structural and response properties of all $BaTiO_3$ phases from density functional theory using the projector-augmented-wave methods. *Computational Materials Science*, 117:306–314, 2016.

[48] Zhicheng Zhong, Anna Tóth, and Karsten Held. Theory of spin-orbit coupling at $LaAlO_3/SrTiO_3$ interfaces and $SrTiO_3$ surfaces. *Physical Review B—Condensed Matter and Materials Physics*, 87(16):161102, 2013.

[49] Saeedeh Farokhipoor and Beatriz Noheda. Conduction through 71 domain walls in $BiFeO_3$ thin films. *Physical Review Letters*, 107(12):127601, 2011.

[50] Yifan Zhu and et al. Ferroelectric domain-wall logic units. *Nature Communications*, 13(1):3349, 2022.

[51] Hanqing Tao and et al. Memory devices based on conducting domain walls in ferroelectric nano-islands. *Advanced Electronic Materials*, 9(1):2200823, 2023.

[52] Wei Li and Dennis Meier. Roadmap for ferroelectric domain wall nanoelectronics. *Advanced Functional Materials*, 31(26):2100250, 2021.

[53] CT Nelson and et al. Domain-wall nanoelectronics. *Reviews of Modern Physics*, 84(1):119–157, 2012.